Journal of Fluids and Structures 127 (2024) 104135

Contents lists available at ScienceDirect

Journal of Fluids and Structures

journal homepage: www.elsevier.com/locate/jfs

Identification of low-wavenumber wall pressure field beneath a turbulent boundary layer using vibration data

Hesam Abtahi [a,*], Mahmoud Karimi [a], Laurent Maxit [b]

[a] Center for Audio, Acoustics and Vibration, University of Technology Sydney, Sydney, Australia
[b] INSA Lyon, Laboratoire Vibrations-Acoustique (LVA), UR677, 25 bis, av. Jean Capelle, F-69621, Villeurbanne Cedex, France

ARTICLE INFO

Keywords:
Turbulent boundary layer
Wall pressure fluctuations
Accelerometer array
Low-wavenumber domain
Flow-induced vibration

ABSTRACT

Although the most energetic part of the wall pressure field (WPF) beneath a turbulent boundary layer (TBL) is within the convective region, this region is mostly filtered out by the structure when excited by a low Mach number turbulent flow. Therefore, structural vibration is primarily induced by the low-wavenumber components of the WPF. This highlights the importance of an accurate estimation of the low-wavenumber WPF for predicting flow-induced vibration of structures. Existing semi-empirical TBL models for the WPF agree well in the convective region but significantly differ from one another in estimating the low-wavenumber levels. In this study, we aim to investigate the feasibility of estimating the low-wavenumber WPF by analyzing vibration data from a structure excited by a TBL. The proposed approach is based on the relationship between the TBL forcing function and structural vibrations in the wavenumber domain. By utilizing vibration data obtained from a structure excited by a TBL and incorporating the sensitivity functions of the respective structure, it is possible to estimate the cross-spectrum density of the pressure fluctuations in the wavenumber domain. To demonstrate the effectiveness of the proposed method, an analytical model of a simply-supported panel excited by a reference TBL model is employed. The vibration data of the panel is then used in an inverse method to identify the low-wavenumber levels of the pressure fluctuations, which are then compared to those of the reference TBL model. The performance of the proposed method is examined through a parametric study and virtual experiments.

1. Introduction

A fluid flowing over the surface of a structure can produce a TBL. The pressure field beneath a TBL excites the structure and causes the structure to vibrate. These flow-induced vibrations might lead to structural fatigue, flutter and aeroelastic instability. Moreover, these vibrations generate sound waves that radiate noise away from the structure into the surrounding environment, impacting acoustic comfort and overall environmental quality. Therefore, it is important to understand how structures react to a TBL excitation. This understanding will enable effective design strategies to minimize flow-induced vibrations, leading to a more favorable acoustic environment and improved overall environmental quality.

To accurately predict flow-induced noise and vibrations, an accurate estimation of the WPF is required. A significant portion of the TBL energy is primarily transmitted through pressure fluctuations at the convective wavenumber, $k_c = \omega/U_c$, where ω is the angular frequency and U_c being the velocity of convection or the average speed of eddies in the boundary layer. Fig. 1 shows a schematic of the cross-spectrum density (CSD) of the TBL wall pressure fields, $\phi_{p_b p_b}(k, \omega)$, and vibration modal response of the

* Corresponding author.
E-mail address: Seyedhesamaldin.abtahi@student.uts.edu.au (H. Abtahi).

https://doi.org/10.1016/j.jfluidstructs.2024.104135
Received 29 January 2024; Received in revised form 3 April 2024; Accepted 14 May 2024
Available online 24 May 2024

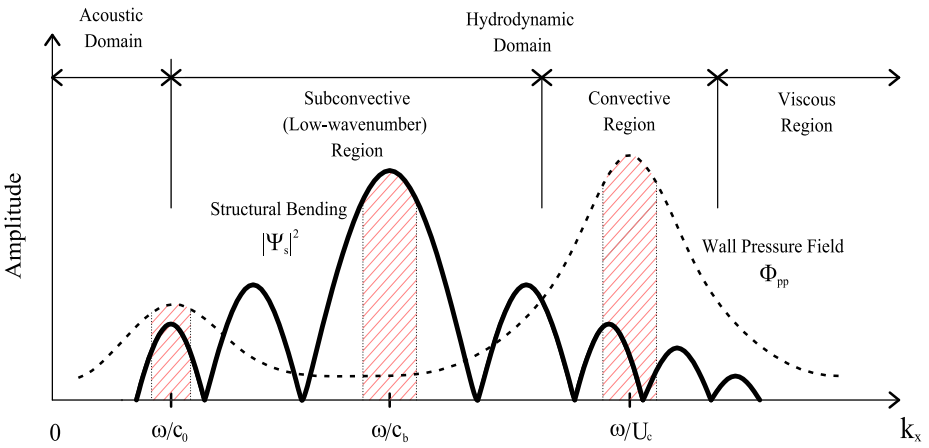

Fig. 1. Schematic of the spatial matching of the wavenumber-frequency spectrum of the TBL WPF and vibration modal function when $U_c < c_b < c_0$ (not in scale). The solid thick line represents the squared magnitude of the structural mode shape, while the dashed line represents the WPF (Abtahi et al., 2024).

structure, $\Psi_s(k,\omega)$. In this figure, the acoustic wavenumber and flexural wavenumber are denoted as $k_0 = \omega/c_0$ and $k_b = \omega/c_b$, respectively, where c_0, c_b are the sound speed and the bending wave speed, respectively. As shown in Fig. 1, the CSD of the WPF can be mainly characterized by two distinct regions: the convective region and the sub-convective region. Vibration response of the structure can be mathematically determined by integrating the product of the WPF CSD function and modal response of the structure in the wavenumber domain (Ciappi et al., 2021).

While the peak energy in the TBL is concentrated around the convective wavenumber, it is recognized that in low Mach number flows related to marine applications, the primary source of structural vibration arises from the low-wavenumber components of the WPF (Hambric et al., 2004; Ciappi et al., 2009; Bonness et al., 2010). The reason is that the structure acts as a filter, attenuating the excitation from the convective ridge of the TBL at frequencies well above the coincidence frequency (the frequency at which the bending wave speed in the structure and the convection speed are equal (Lecoq et al., 2014)). As a result, the vibration induced by the TBL is primarily governed by the low-wavenumber portion of the WPF (Martin and Leehey, 1977; Hwang and Maidanik, 1990). This was confirmed by Hambric et al. (2004) and Hwang and Maidanik (1990), who investigated the vibration response of a baffled flat rectangular plate with various boundary conditions under a low-speed TBL flow excitation. The study revealed that a plate with simply supported or clamped boundary conditions significantly filters out the contribution of the TBL convective ridge to its vibrational response and at high frequencies, where the flexural wavenumber of the plate was lower than the convective wavenumber, the response of the plate with these boundary conditions was mostly due to the wall pressure energy in the low-wavenumber region. This highlights the importance of the low-wavenumber WPF in the prediction of flow-induced vibrations.

Over the past 50 years, researchers have developed several semi-empirical TBL models, with varying degrees of accuracy, aimed at estimating the WPF beneath a TBL (Keith et al., 1992; Hwang et al., 2003; Miller et al., 2012). Two types of TBL models have been developed to fully define the TBL WPF namely the auto-spectrum or single point spectrum model and normalized CSD model. The former represents the energy of the pressure fluctuations using mean square pressure fluctuations. Goody's model is a well-known example of this type, showing very good agreement with experimental data under zero pressure gradients (Goody, 2004). The latter describes pressure energy distribution based on wavelength. Notable examples of such TBL models include the Corcos (1964), Chase (1980), Mellen (1990) and Smol'yakov (2000) wavenumber-frequency models. Fig. 2 displays the normalized TBL pressure spectrum level of these models as a function of non-dimensional wavenumber for $k_y = 0$. These models rely on theoretical principles and have been developed based on numerous experimental measurements and data fittings.

All the semi-empirical models have been developed based on acoustic measurements, which involve using a microphone array to directly measure the sound waves generated by the TBL pressure fluctuations. To estimate the TBL WPF, the recorded sound signals are processed using techniques like Fourier transform, beamforming, or other signal processing methods to extract information about the wall pressure fluctuations (Maidanik, 1967; Blake and Chase, 1971; Geib and Farabee, 1976). One difficulty with these acoustic measurements is that to avoid aliasing effect, the sensor spacing should be small enough to distinguish the smallest turbulent scales (Ciappi et al., 2021). This means high-density microphone arrays are usually required (Arguillat et al., 2010). Recently, Damani et al. (2022) utilized a Kevlar-covered acoustic resonator-based cavity sensor for capturing the low-wavenumber components of WPF beneath a TBL flow. However, the membrane-like characteristics of the Kevlar scrim indicate a gradual decrease in sensitivity towards the edges of the sensors, posing a challenge in optimizing these sensors for sub-convective pressure measurements. Recognizing the limitations of Kevlar-covered sensors, Damani et al. (2024) pursued an alternative approach by employing multiple-neck Helmholtz resonator-based sensors. They investigated a measurement technique utilizing large sensors and a large array. Comparisons with existing wall pressure models, they revealed that pressure levels in the low-wavenumber domain are 45 dB lower than the convective pressures. The low amplitude of WPF in the low-wavenumber domain, compared to the amplitude

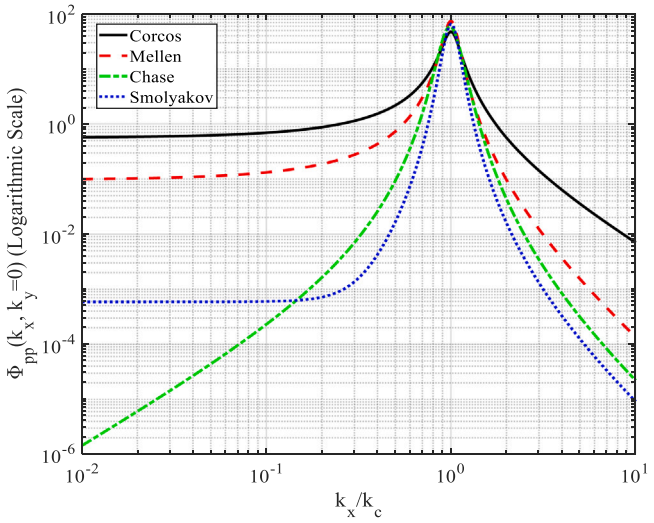

Fig. 2. Normalized TBL pressure spectrum levels as a function of non-dimensional wavenumber for $k_y = 0$ at $f = 3000$ Hz for four different models. k_x and k_y represent the streamwise and spanwise wavenumbers, respectively, and k_c is the convective wavenumber.

of the WPF at convective wavenumbers, presents another challenge in estimating the low-wavenumber components of the WPF from acoustic measurements. This is why there is a notable discrepancy in the sub-convective region among all the four models in Fig. 2, while they show good agreement in predicting pressure fluctuations within the convective region. For more information, the readers are referred to the authors' recent publication, where they have presented a thorough investigation of the estimation of the low-wavenumber WPF using an acoustic-based approach and have discussed associated challenges and difficulties with the estimation process (Abtahi et al., 2024).

To tackle the challenges arising from estimating the sub-convective domain of the WPF using the acoustic-based approach, a vibration-based approach is proposed herein. This alternative approach involves measuring the vibrations of a structure excited by a TBL, and then using the measured data to reconstruct the low-wavenumber WPF. This approach takes advantage of the structure's wavenumber filtering capabilities, reducing contamination of the low-wavenumber domain by the convective region as it occurs in the acoustic approaches. Another benefit of this approach is that it is non-intrusive as the accelerometers can be placed on the side of the structure opposite to the one excited by the fluid flow, therefore not impacting the turbulent flow. Consequently, there is no need to drill holes in the structure to have flush-mounted sensors as required by the acoustic-based approach.

Jameson (1975) pioneered the use of a vibration-based approach to measure the amplitude of the WPF in the low-wavenumber domain. Employing a carefully designed rectangular clamped plate, he minimized contributions from the convective peak of the TBL pressure, ensuring that the low-wavenumber components of the WPF matched the wavenumber of the plate's bending waves. Jameson made the assumption that the spectral density in the low-wavenumber frequency domain is symmetric (i.e. in k_x, k_y, and ω). He utilized the individual modes of the clamped plate to create a theoretical framework for the average power within each mode. Subsequently, he employed the accelerometer output as an indicator of modal response to estimate the level of the low-wavenumber spectral components in the TBL wall pressure. In 1977, Martin and Leehey employed a flexible membrane excited by a turbulent airflow as a spatial filter to capture the wavenumber components of the WPF, specifically focusing on ranges far below the convective region but above the acoustic region (Martin and Leehey, 1977). In their experiment, they used a non-contact optical sensor to monitor the displacement response at the center of the membrane. They assumed that the WPF in the low-wavenumber range is uniformly flat. By applying spatial Fourier transformation to the observed mode shape, they effectively translated the modal response to the wavenumber domain. Subsequently, they computed the low-wavenumber components of unsteady surface pressure based on the spatial-wavenumber response of the structure and its resonance characteristics. Finally, they compared the measured displacement response with data from modal analysis of the membrane. Comparing the estimated low-wavenumber WPF in the Martin and Leehey's work to those obtained by Blake and Chase (1971) in the same wind tunnel and Jameson (1970) using an acoustic-based approach, it was observed that the Blake's estimation exceeded the magnitude of the Martin and Leehey's estimated WPF in the low-wavenumber domain. Whereas, the estimated low-wavenumber WPF by Martin and Leehey surpassed that of Jameson's.

These studies laid the foundation for subsequent experiments. For instance, Bonness et al. (2010) and Evans et al. (2013) estimated the TBL surface pressure levels at low-wavenumbers for both smooth and rough surfaces. They used an accelerometer array mounted on external surface of a water pipe, and then the measured vibration of the pipe due to the internal WPF excitation was used in an iterative inverse method to identify the WPF. In order to compute the modal force, they assumed a constant pressure spectrum level in the low-wavenumber range around the modal wavenumber. An analytical formulation for the modal force as a function of the TBL wavevector-frequency spectrum and the computed sensitivity function (obtained from experimental modal analysis) were used. This was then used to compute the frequency response function for each individual mode. Next, the low-wavenumber TBL

pressure levels were fine-tuned to align the computed vibration data with the measured data. Finally, the measured low-wavenumber pressure data was compared with findings from other studies. The results for the smooth pipe indicated that the measured data fell between the predicted results from the TBL models by Chase (1992) and Smol'Yakov (2006), registering a few decibels below the lower bounds reported in related measurements in air by Farabee and Geib (1975) and Martin and Leehey (1977). However, the pressure levels for fully rough conditions exhibited a 13 dB increase in low-wavenumber wall pressure compared to a hydraulically smooth surface.

In most of the previous studies using vibration-based approaches, it was assumed that the WPF level in the low-wavenumber domain is constant. Furthermore, once the low-wavenumber WPF was estimated, there was no reference WPF to ensure that obtained results were accurate. This highlights the necessity for further study not only to improve the process of identification of the low-wavenumber WPF but also to verify its effectiveness before employing it in practice. This is only possible if the estimated WPF could be benchmarked against a known input TBL WPF in the low-wavenumber domain. Thus, in this work, an inverse vibration approach, which relates structural vibrations to the TBL forcing function, is initially proposed. The proposed method is then implemented in a numerical study to verify the estimated WPF against an input reference TBL WPF modeled by semi-empirical models. Additionally, a virtual vibration experiment is utilized to mimic experimental conditions. Through this virtual model, challenges related to the application of the vibration-based approach in experimentally estimating the low-wavenumber WPF have been evaluated.

The structure of the paper is as follows: In Section 2, the methodology for estimating the WPF is outlined. This method is then employed to estimate the WPF in the low-wavenumber domain in Section 3, where the results obtained using the closed-form semi-empirical TBL model and virtual vibration experiment are compared. The solution procedure, along with the estimated WPF in the low-wavenumber domain, is discussed in Section 3.1. This subsection examines the effect of number of sensors and plate dimensions on the estimation of the WPF in the low-wavenumber domain. This analysis is conducted while considering a closed-form semi-empirical TBL model as the input exciting force. Next, the process for virtual experiments is detailed in Section 3.2, and the impact of the number of realizations/snapshots needed for a reliable estimation of the low-wavenumber WPF is investigated. Finally, the paper concludes with a discussion in Section 4 and a summary of the findings.

2. Methodology

This section is divided into three subsections. In Section 2.1, we introduce an inverse vibration approach employed to estimate the TBL WPF in the low wavenumber domain based on vibration data from the excited panel. This section describes the relation between the CSD of the WPF expressed in the wavenumber domain and the CSD of the panel acceleration at various points. The accuracy of the proposed method is evaluated through comparison with reference results. The CSD of the TBL WPF is simulated in two different ways. The first way, discussed in Section 2.2, involves using closed-form semi-empirical models as an input forcing function. This analysis enables us to examine the impact of various parameters on the performance of the proposed method. The second way, outlined in Section 2.3, involves simulating the input force using different realizations/snapshots. To simulate an experiment, various realizations of the WPF will be generated using the uncorrelated wall plane wave (UWPW) technique (Maxit, 2016). This approach allows for an investigation into the influence of the number of snapshots required for reliable estimation of low-wavenumber WPF.

2.1. Inverse vibration method

In this section, an inverse vibration method is proposed to estimate the TBL WPF in the low-wavenumber domain from vibration data. Let us consider a flat panel excited by a TBL. We assume that the TBL is homogeneous, stationary, and fully developed across the panel surface, and that the vibration of the panel does not influence the WPF. Fig. 3 illustrates the considered system for the numerical applications presented in this paper: the panel is rectangular and simply-supported on its four edges. An array of N_s virtual accelerometers is mounted on the panel to measure the vibrations. The x-axis is considered parallel to the streamwise direction, and the free stream velocity is denoted by U_∞. The panel has the density of ρ_s, length of L_x and width of L_y, and bending stiffness of $D = Eh^3/(12(1-\nu^2))$, where h is the panel thickness, E is the Young's modulus and ν is Poisson's ratio. The Kirchhoff theory is considered here to represent the motions of the considered thin panel, and to calculate the acceleration of the panel (Rao, 2019).

The panel acceleration at point $\mathbf{x}$, $\gamma(\mathbf{x},t)$ induced by the WPF, can be expressed as the convolution product (Maury et al., 2002)

$$\gamma(\mathbf{x},t) = \iint_{\sum_p} \int_{-\infty}^{\infty} h_\gamma(\mathbf{x},\tilde{\mathbf{x}},t-\tau)p(\tilde{\mathbf{x}},\tau)\,\mathrm{d}\tau\mathrm{d}\tilde{\mathbf{x}}, \tag{1}$$

where $p(\tilde{\mathbf{x}},\tau)$ is the WPF exerted on the surface of the panel $\sum_p$, and $h_\gamma(\mathbf{x},\tilde{\mathbf{x}},t)$ is the acceleration impulse response at point $\mathbf{x}$ due to a normal unit force at point $\tilde{\mathbf{x}}$.

Due to the random nature of the turbulent flow, the panel response can be described by the cross-correlation function of the acceleration between two points $\mathbf{x}$ and $\mathbf{x}'$, denoted as $R_{\gamma\gamma}$. Assuming a stationary and ergodic random process, $R_{\gamma\gamma}$ can be expressed as follows

$$R_{\gamma\gamma}(\mathbf{x},\mathbf{x}',t) = \int_{-\infty}^{\infty} \gamma(\mathbf{x},t)\gamma(\mathbf{x}',t+\tau)\,\mathrm{d}\tau. \tag{2}$$

By substituting Eq. (1) into Eq. (2) and performing a temporal Fourier transform on the cross-correlation function of the panel acceleration, the space-frequency spectrum of the panel acceleration, $S_{\gamma\gamma}(\mathbf{x},\mathbf{x}',\omega)$, can be computed as follows (Maury et al., 2002)

$$S_{\gamma\gamma}(\mathbf{x},\mathbf{x}',\omega) = \iint_{\sum_p} \iint_{\sum_p} H_\gamma(\mathbf{x},\tilde{\mathbf{x}},\omega)S_{pp}(\tilde{\mathbf{x}},\tilde{\tilde{\mathbf{x}}},\omega)H_\gamma^*(\mathbf{x}',\tilde{\tilde{\mathbf{x}}},\omega)\,\mathrm{d}\tilde{\mathbf{x}}\mathrm{d}\tilde{\tilde{\mathbf{x}}}, \tag{3}$$

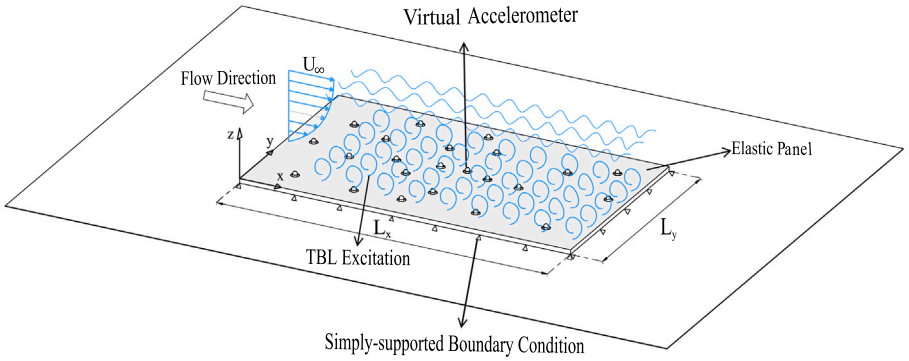

Fig. 3. Schematic of a random accelerometer array mounted on an elastic simply-supported panel to measure acceleration response of the panel excited by wall pressure fluctuations beneath the turbulent boundary layer.

where $H_\gamma(\mathbf{x}, \tilde{\mathbf{x}}, \omega)$ is the acceleration at point $\mathbf{x}$ for a normal force at point $\tilde{\mathbf{x}}$, $S_{pp}(\tilde{\mathbf{x}}, \tilde{\tilde{\mathbf{x}}}, \omega)$ is the temporal Fourier transform of the cross-correlation function of the WPF, and the asterisk denotes the complex conjugate. The space-frequency spectrum of $S_{pp}(\tilde{\mathbf{x}}, \tilde{\tilde{\mathbf{x}}}, \omega)$, can be expressed as follows by applying the inverse Fourier transform to the CSD function of TBL pressure in the wavenumber domain, $\phi_{pp}(\mathbf{k}, \omega)$,

$$S_{pp}(\tilde{\mathbf{x}}, \tilde{\tilde{\mathbf{x}}}, \omega) = \frac{1}{4\pi^2} \iint_{-\infty}^{\infty} \phi_{pp}(\mathbf{k}, \omega) e^{\mathrm{j}\mathbf{k}(\tilde{\tilde{\mathbf{x}}} - \tilde{\mathbf{x}})} \, \mathrm{d}\mathbf{k}, \tag{4}$$

where $\mathrm{j} = \sqrt{-1}$ is the imaginary unit, $\mathbf{k}$ is the wavevector with components k_x and k_y in the streamwise and spanwise directions in the (x, y) plane, respectively. By substituting Eq. (4) into Eq. (3) and rearranging the terms, one obtains

$$S_{\gamma\gamma}(\mathbf{x}, \mathbf{x}', \omega) = \frac{1}{4\pi^2} \iint_{-\infty}^{\infty} H_\gamma(\mathbf{x}, \mathbf{k}, \omega) \phi_{pp}(\mathbf{k}, \omega) H_\gamma^*(\mathbf{x}', \mathbf{k}, \omega) \, \mathrm{d}\mathbf{k}, \tag{5}$$

where

$$H_\gamma(\mathbf{x}, \mathbf{k}, \omega) = \iint_{\Sigma_p} H_\gamma(\mathbf{x}, \tilde{\mathbf{x}}, \omega) e^{-\mathrm{j}\mathbf{k}\tilde{\mathbf{x}}} \, \mathrm{d}\tilde{\mathbf{x}}. \tag{6}$$

$H_\gamma(\mathbf{x}, \mathbf{k}, \omega)$ characterizes the vibration behavior of the panel and is called sensitivity function. Eq. (6) indicates that $H_\gamma(\mathbf{x}, \mathbf{k}, \omega)$ is the acceleration at point $\mathbf{x}$ when the panel is excited by a unit wall plane wave of wavevector $\mathbf{k}$. The sensitivity function for a simply-supported panel is given in Appendix.

Let us consider N_s accelerometers mounted on the panel surface excited by a TBL, see Fig. 3. The position of each accelerometer is determined by the coordinates $\mathbf{x}_i$, denoted as (x_i, y_i) for $i \in \{1, N_s\}$. By truncating and sampling the wavenumber space, and employing the rectangular rule to approximate the integration in Eq. (5), one can compute the CSD of panel acceleration between two points $\mathbf{x}_i$ and $\mathbf{x}_j$ as follows

$$S_{\gamma\gamma}(\mathbf{x}_i, \mathbf{x}_j, \omega) = \frac{1}{4\pi^2} \sum_{l=1}^{N_k} H_\gamma(\mathbf{x}_i, \mathbf{k}_l, \omega) \phi_{pp}(\mathbf{k}_l, \omega) H_\gamma^*(\mathbf{x}_j, \mathbf{k}_l, \omega) \, \delta k_x \delta k_y, \tag{7}$$

where δk_x and δk_y denote the resolutions of the wavenumber domain in the streamwise and spanwise directions, respectively. The total number of points in the wavenumber space is denoted by $N_k = N_{k_x} \times N_{k_y}$, where N_{k_x} and N_{k_y} indicate the number of points considered in sampling the wavenumber space along the x and y axes, respectively. The wavevector at a discrete point l is represented by $\mathbf{k}_l = (k_{x,l}, k_{y,l})$.

For the given array of N_s sensors, we define the CSD of the panel acceleration between each $N_s \times N_s$ combination of sensors as $S_{\gamma\gamma}(\mathbf{x}_i, \mathbf{x}_j, \omega)$, where $i, j \in \{1, N_s\}$. Then, all computed CSD of accelerations are stored in a vector denoted as $\mathbf{S}_\gamma$, referred to as the acceleration CSD vector. The components of $\mathbf{S}_\gamma$ are organized such that the first N_s components correspond to $S_{\gamma\gamma}(\mathbf{x}_1, \mathbf{x}_j, \omega)$ with $j \in \{1, N_s\}$, the next N_s components correspond to $S_{\gamma\gamma}(\mathbf{x}_2, \mathbf{x}_j, \omega)$ with $j \in \{1, N_s\}$, and so on:

$$\mathbf{S}_\gamma = \begin{bmatrix} S_{\gamma\gamma}(\mathbf{x}_1, \mathbf{x}_1, \omega) \\ S_{\gamma\gamma}(\mathbf{x}_1, \mathbf{x}_2, \omega) \\ \vdots \\ S_{\gamma\gamma}(\mathbf{x}_i, \mathbf{x}_j, \omega) \\ \vdots \\ S_{\gamma\gamma}(\mathbf{x}_{N_s}, \mathbf{x}_{N_s-1}, \omega) \\ S_{\gamma\gamma}(\mathbf{x}_{N_s}, \mathbf{x}_{N_s}, \omega) \end{bmatrix}_{N_s^2 \times 1}. \tag{8}$$

As the CSD of the panel acceleration between different sensors can be estimated by Eq. (7), we can then write it in the following compact format

$$\mathbf{S}_\gamma = \mathbf{Q}\boldsymbol{\Phi}_{\mathbf{pp}}, \tag{9}$$

where $\boldsymbol{\Phi}_{\mathbf{pp}}$ is a vector consisting of the unknown WPF components in the truncated wavenumber space as follows

$$\boldsymbol{\Phi}_{\mathbf{pp}} = \begin{bmatrix} \phi_{pp}(k_{x,1}, k_{y,1}, \omega) \\ \phi_{pp}(k_{x,1}, k_{y,2}, \omega) \\ \vdots \\ \phi_{pp}(k_{x,l}, k_{y,l}, \omega) \\ \vdots \\ \phi_{pp}(k_{x,N_{k_x}}, k_{y,N_{k_y}-1}, \omega) \\ \phi_{pp}(k_{x,N_{k_x}}, k_{y,N_{k_y}}, \omega) \end{bmatrix}_{N_k \times 1}. \tag{10}$$

The components of $\boldsymbol{\Phi}_{\mathbf{pp}}$ are organized such that the first N_{k_y} components correspond to $\phi_{pp}(k_{x,1}, k_{y,l}, \omega)$ with $l \in \{1, N_{k_y}\}$, the next N_{k_y} components correspond to $\phi_{pp}(k_{x,2}, k_{y,l}, \omega)$ with $l \in \{1, N_{k_y}\}$, and so on. Besides, $\mathbf{Q}$ is a matrix with the following elements

$$\mathbf{Q} = \frac{\delta k_x \delta k_y}{4\pi^2} \times \begin{bmatrix} H_\gamma(\mathbf{x}_1, \mathbf{k}_1, \omega)H_\gamma^*(\mathbf{x}_1, \mathbf{k}_1, \omega) & H_\gamma(\mathbf{x}_1, \mathbf{k}_2, \omega)H_\gamma^*(\mathbf{x}_1, \mathbf{k}_2, \omega) & \cdots & \cdots & H_\gamma(\mathbf{x}_1, \mathbf{k}_{N_k}, \omega)H_\gamma^*(\mathbf{x}_1, \mathbf{k}_{N_k}, \omega) \\ H_\gamma(\mathbf{x}_1, \mathbf{k}_1, \omega)H_\gamma^*(\mathbf{x}_2, \mathbf{k}_1, \omega) & \ddots & & & \vdots \\ \vdots & & H_\gamma(\mathbf{x}_i, \mathbf{k}_l, \omega)H_\gamma^*(\mathbf{x}_j, \mathbf{k}_l, \omega) & & \vdots \\ \vdots & & & \ddots & H_\gamma(\mathbf{x}_{N_s}, \mathbf{k}_{N_k}, \omega)H_\gamma^*(\mathbf{x}_{N_s-1}, \mathbf{k}_{N_k}, \omega) \\ H_\gamma(\mathbf{x}_{N_s}, \mathbf{k}_1, \omega)H_\gamma^*(\mathbf{x}_{N_s}, \mathbf{k}_1, \omega) & \cdots & \cdots & & H_\gamma(\mathbf{x}_{N_s}, \mathbf{k}_{N_k}, \omega)H_\gamma^*(\mathbf{x}_{N_s}, \mathbf{k}_{N_k}, \omega) \end{bmatrix}_{N_s^2 \times N_k}. \tag{11}$$

The elements of matrix $\mathbf{Q}$ can be acquired through experiments or numerical simulations. At a specific excitation frequency, the vector $\mathbf{S}_\gamma$ can also be calculated based on the panel vibration response to the TBL forcing function. According to Eq. (9), we arrive at N_s^2 equations for the $N_x \times N_y$ unknown coefficients. In most cases, the number of unknowns $N_x \times N_y$ exceeds the number of equations N_s^2. Eq. (9) is therefore an under-determined system, and it has no unique solution. Moreover, $\mathbf{Q}$ in Eq. (9) is a non-square matrix, and standard inversion cannot be applied to the matrix. Hence, the goal is to find an approximate solution of $\phi_{pp}(\mathbf{k}, \omega)$ that minimizes the residuals of the Eq. (9). For this purpose, a regularization technique can be used as a pseudo-inverse method to estimate the WPF in the low-wavenumber domain (Hansen, 2007). Consequently, the wall pressure CSD vector for that particular frequency can be approximated as follows

$$\boldsymbol{\Phi}_{\mathbf{pp}} = [\mathbf{Q}]^\dagger \mathbf{S}_\gamma, \tag{12}$$

where † denotes the pseudo-inverse.

Performance of the proposed method can be numerically evaluated by benchmarking the estimated WPF against a reference input WPF. This can be done by exciting the panel through a known forcing function and applying Eq. (12) to the computed vibration response. Therefore, modeling the reference TBL forcing function is very important in the performance evaluation of the proposed method. In Sections 2.2 and 2.3, we have described two ways of simulating the reference TBL forcing functions, which allow us to study the efficacy of the proposed method in both ideal and practical situations.

2.2. Closed-form CSD of the wall pressure field

In this subsection, we have detailed the process of simulating the reference TBL forcing function using the closed-form semi-empirical models. The CSD of the WPF in Eq. (5) can be determined as per Graham formulation (Graham, 1996, 1997) by utilizing different models for auto-spectral density (ASD) of the pressure field, $\Psi_{pp}(\omega)$, and the normalized CSD of the pressure field, $\tilde{\phi}_{pp}(k, \omega)$, independently, as stated below

$$\phi_{pp}(\mathbf{k}, \omega) = \Psi_{pp}(\omega) \left(\frac{U_c}{\omega}\right)^2 \tilde{\phi}_{pp}(\mathbf{k}, \omega). \tag{13}$$

Among various semi-empirical models developed for simulation of ASD of WPF, many works showed that the Goody model is more compatible with experimental data compared to other models (Hwang et al., 2009; Miller et al., 2012). Thus, the Goody model (Goody, 2004) is used in this paper to assess the ASD function of the WPF in Eq. (13),

$$\Psi_{pp}(\omega) = \frac{3\tau_\omega^2 \delta \left(\frac{\omega\delta}{U_e}\right)^2}{U_e \left(0.5 + \left(\frac{\omega\delta}{U_e}\right)^{0.75}\right)^{3.7} \left(1.1 R_T^{-0.57} \left(\frac{\omega\delta}{U_e}\right)\right)^7}, \tag{14}$$

where $R_T = U_\tau^2 \delta / U_e \nu$ and U_e is the boundary layer edge velocity. It is worth mentioning that $\Psi_{pp}(\omega)$ represents a one-sided radial frequency spectrum. Therefore, to transform it into a cyclic frequency spectrum density $\Psi_{pp}(f)$, it is multiplied by 2π. Various semi-empirical models have been developed for the normalized CSD function (Miller et al., 2012). For example, the Corcos model stands out as the most popular model. However, it is well known that the Corcos model tends to overpredict the amplitude of the low-wavenumber domain (Juvé et al., 2019). The Mellen model offers more realistic predictions for low-wavenumber levels. This has been confirmed by comparisons between the vibration responses of a plate excited by a TBL modeled using the Corcos/Mellen models and experimental data (Karimi et al., 2020a). Therefore, in this study, the normalized CSD function was obtained using the Mellen model (Mellen, 1990) as follows

$$\tilde{\phi}_{pp}(k_x, k_y, \omega) = \frac{2\pi \left(\alpha_x \alpha_y\right)^2 k_c^3}{\left(\alpha_x \alpha_y k_c\right)^2 + \left(\alpha_x k_y\right)^2 + \left(\alpha_y^2 \left(k_x - k_c\right)^2\right)^{3/2}}, \tag{15}$$

where $\alpha_x = 0.1$ and $\alpha_y = 0.77$. Also, the convection velocity U_c is approximated as follows (Hambric et al., 2004)

$$U_c \approx U_\infty \left(0.59 + 0.3 e^{-0.89\delta^* \omega / U_\infty}\right), \tag{16}$$

where δ^* is the TBL displacement thickness.

In order to calculate the panel acceleration using the closed-form semi-empirical models in Eq. (7), a truncated number of wavenumbers in the x and y directions need to be defined. When defining the cut-off wavenumbers in these directions, it is important to ensure that the range of considered wavenumbers is large enough to be able to include the significant contribution of the CSD function. For this study, a cut-off wavenumber of $1.2k_c$ was used in both directions to account for the convective contributions of the WPF of the TBL simulated using the Goody+Mellen model. It is noteworthy mentioning that a convergence study has been performed to select the cut-off wavenumber and identify the wavenumber resolution in the wavenumber domain to ensure that the input TBL is accurately modeled and the estimated wall pressure field is converged.

2.3. Realizations of the wall pressure field

A closed-form formula for the TBL WPF does not exist in practice, and only a limited number of snapshots/samples is available. Therefore, we have introduced a second procedure in this subsection, which involves a virtual model specifically designed for conducting vibration experiments. To do this, a random TBL is simulated with deterministic loading using the UWPW technique (Maxit, 2016), which mimics experimental situations. This virtual experiment synthesizes TBL wall pressure and then uses this deterministic forcing function to calculate the acceleration response of a panel using the ensemble average of different realizations of wall pressure. The pressure beneath the TBL for the rth realization can be represented by a set of UWPWs at point (x_M, y_M) of the panel as follows (Maxit, 2016; Karimi et al., 2019, 2020a).

$$p^r(x_M, y_M, \omega) = \sum_{l=1}^{N_k} \sqrt{\frac{\phi_{pp}(k_{x,l}, k_{y,l}, \omega)\delta k_x \delta k_y}{4\pi^2}} e^{\mathrm{j}(k_{x,l} x_M + k_{y,l} y_M + \theta_l^r)}, \tag{17}$$

where θ is a random phase uniformly distributed in $[0\,2\pi]$. Using the modal expansion method (as described in Appendix for evaluation of the sensitivity functions), the acceleration response of a panel at point (x_M, y_M) at a given frequency of ω induced by the wall pressure (Eq. (17)) corresponding to the rth realization at each sensor position can be obtained by Maxit (2016) (see Appendix for the notation),

$$\gamma^r(x_M, y_M, \omega) = -\omega^2 \sum_{m=1}^{M} \sum_{n=1}^{N} \frac{F_{mn}^r(\omega) \varphi_{mn}(x_M, y_M)}{\Omega(\omega_{mn}^2 - \omega^2 + \mathrm{j}\eta\omega\omega_{mn})}, \tag{18}$$

where the modal forces are given by

$$F_{mn}^r = \sum_{l=1}^{N_k} \sqrt{\frac{\phi_{pp}(k_{x,l}, k_{y,l}, \omega)\delta k_x \delta k_y}{4\pi^2}} e^{\mathrm{j}\theta_l^r} \psi_{mn}(k_{x,l}, k_{y,l}). \tag{19}$$

In the following section, we assess the results obtained from employing the proposed approach to estimate the WPF in the low-wavenumber domain.

3. Results and discussion

This section uses the formulation outlined in Section 2 to evaluate the WPF in the low-wavenumber domain. This study investigates a rectangular steel panel with a simply-supported boundary condition that is excited by a TBL. Table 1 presents the panel's dimensions and material properties. Fig. 3 shows a turbulent airflow with a free flow velocity of 50 m/s moving over the panel. The air density and the kinematic viscosity values are set to 1.225 $\mathrm{kg/m^3}$ and 1.5111×10^{-5} $\mathrm{m^{2/s}}$, respectively. The TBL parameters for the panel are given in Table 2.

Moreover, selecting the wavenumber resolution is pivotal in the WPF calculations, necessitating a balance between computational costs and accuracy. As $\mathbf{Q}$ is dependent on the wavenumber resolution, in this study, we adjust the wavenumber resolution at each frequency to ensure a constant size for matrix $\mathbf{Q}$ across all frequencies. To ensure that the computed CSD of the panel acceleration

Table 1
Dimensions and material properties of the panel.

Parameter	Value
Young's modulus E (Gpa)	210
Poisson's ratio ν	0.3
Density ρ_s (kg/m^3)	7800
Length L_x (mm)	455
Width L_y (mm)	375
Thickness h (mm)	1
Damping loss factor η	0.01
Flexural Wavenumber k_b $(1/m)$	89.46

Table 2
TBL parameters for air flow with speed of 50 m/s.

Parameter	Value
TBL thickness δ (mm)	5.77
TBL displacement thickness δ^* (mm)	0.729
Wall shear stress τ (pa)	5.989

by the virtual accelerometers in both techniques incorporates all major modes, in this study, we employed $M = N = 50$ in calculating $\mathbf{S}_\gamma(\omega)$ in Eq. (7) through Eq. (A.1). However, for computing the $H_\gamma(\mathbf{x}, \mathbf{k}, \omega)$ in Eq. (11), we only consider the modes number of M and N within the frequency range $[0, 1.3\omega]$, as in practice, only the resonant modes in a given frequency band can be reasonably estimated. Furthermore, in order to effectively utilize the structure's wavenumber filtering abilities for estimating the low-wavenumber domain of the WPF through the panel's vibration response, it is essential that the excitation frequency be well above the coincidence frequency. This condition ensures that the convective wavenumber of the TBL excitation remains far from the flexural wavenumber of the panel. The flexural wavenumber k_b of a panel is given by Guyader (2013)

$$k_b = \sqrt[4]{\frac{12\rho_s(1-\nu^2)}{Eh^2}}\sqrt{\omega}. \tag{20}$$

It is important to note that the low-wavenumber domain investigated in this study is defined within the range of the panel's flexural wavenumber ($-k_b \leq k_x, k_y \leq k_b$). The coincidence frequency of the considered panel in this paper is around $f \approx 200$ Hz. Consequently, to apply the vibration approach for estimating the WPF in the low-wavenumber domain, a minimum frequency of $f = 400$ Hz is chosen. This condition ensures that the convective wavenumber of the TBL excitation remains far from the flexural wavenumber of the panel. Hence, the convective domain is filtered out by the structure (see Fig. 1), and this allows us to overcome the main challenge of estimating the low-wavenumber components of the WPF using an acoustic method (Abtahi et al., 2024).

Fig. 4 illustrates the flowchart outlining the three-step procedure employed in this work for estimating the WPF in the low-wavenumber domain. In the first step, the CSD of the panel acceleration is calculated. Here, we have initially simulated the TBL forcing function using both the closed-form semi-empirical models (Section 2.2) and the UWPW technique (Section 2.3). The former employs Eqs. (A.1) and (7) to compute the CSD of the panel accelerations at the sensor positions. This technique provides a theoretical framework for estimating the WPF in an ideal situation and is particularly useful for parametric study and gaining insights into the fundamental behavior of the proposed method (see Section 3.1). However, by utilizing the virtual experiment model (see Section 3.2), it is possible to have a more realistic assessment of the efficiency of using an accelerometer array to estimate the low-wavenumber WPF in real-world situations. To achieve this, Eq. (17) simulates the TBL forcing function using the UWPW technique, and the panel accelerations at the sensor positions are computed using Eq. (18). In the second step, components of matrix $\mathbf{Q}$ are computed by substituting the sensitivity function of the simply-supported panel (Eq. (A.1)) into Eq. (11). In the final step, the regularization technique is applied to Eq. (12) to estimate the low-wavenumber components of the WPF.

3.1. WPF estimation using a closed-form semi-empirical TBL model

The initial step in measuring the acceleration response of the panel excited by a TBL involves arranging sensors. However, practical limitations prevent using a large number of accelerometers. This raises the question of how many sensors are needed to obtain a reasonable estimation of the WPF in the low-wavenumber domain. In this work, we employ a random array of sensors as shown in Fig. 5. Each sensor is numbered to highlight the sensors' location for estimating the WPF in the low-wavenumber domain. For example, when it is stated that 10 or 20 sensors are used in the array, it simply means the sensors from 1 to 10 or 1 to 20 are selected from the 34 sensors shown in Fig. 5. In the upcoming subsections, we examine the impact of the number of sensors on the estimation of WPF in the low-wavenumber domain using two numerical methods: (1) the Moore–Penrose pseudo-inverse method (Ben-Israel and Greville, 2003) and (2) the truncated generalized singular value decomposition (TGSVD) method (Hansen, 2007).

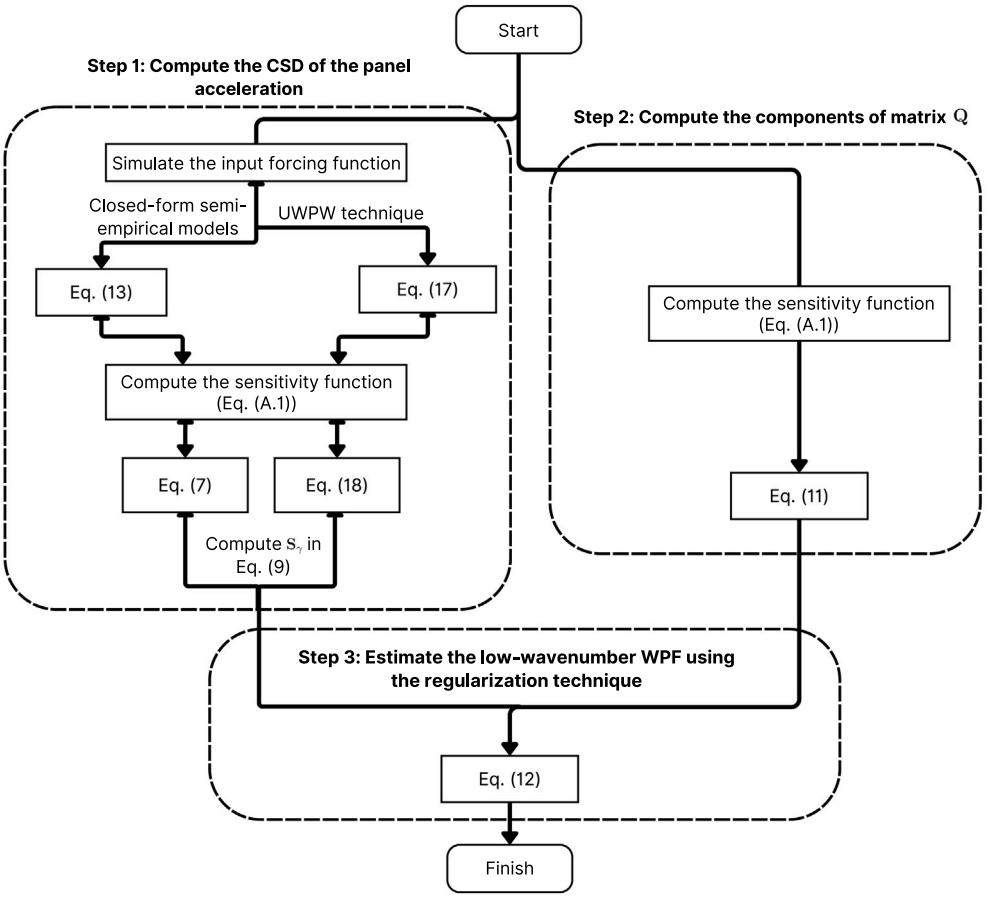

Fig. 4. Flowchart illustrating the procedure for estimating the low-wavenumber WPF.

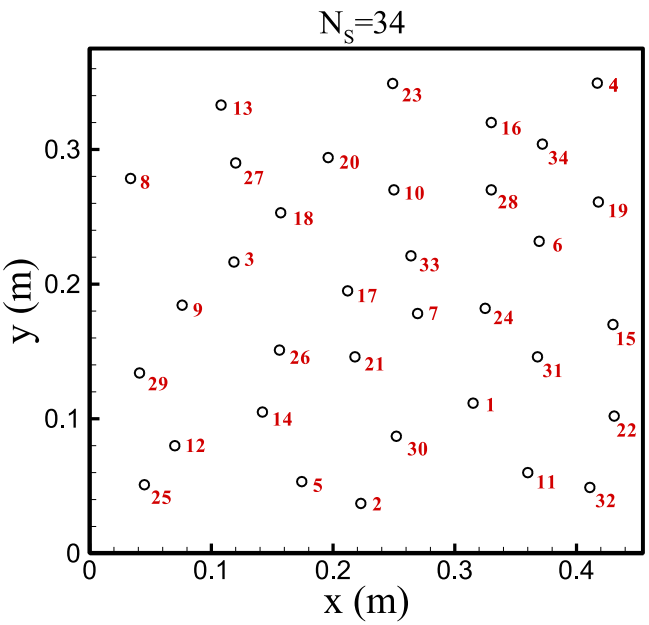

Fig. 5. An irregular array pattern with 34 sensors; *x*-axis in streamwise and *y*-axis in spanwise directions.

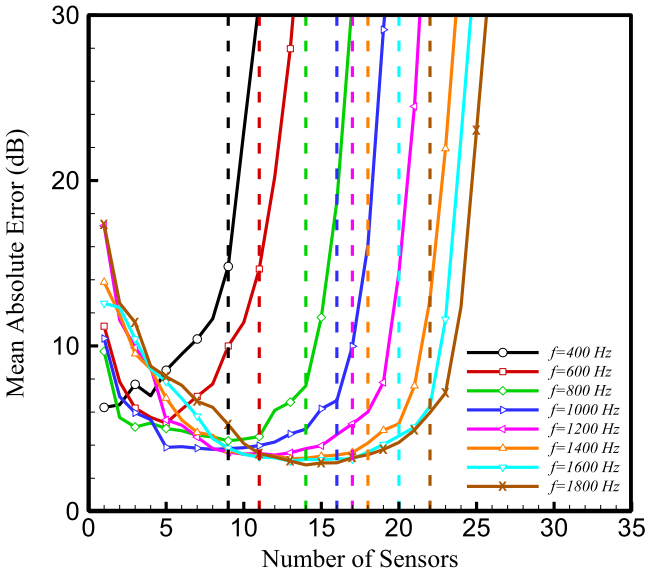

Fig. 6. MAE for estimated WPF in the low-wavenumber domain as a function of number of sensors at some selected frequencies using the Moore–Penrose Pseudo-inverse method.

3.1.1. Moore–Penrose Pseudo-inverse method

To estimate the TBL WPF, Eq. (12) needs to be solved. As a first attempt, the Moore–Penrose pseudo-inverse method (Ben-Israel and Greville, 2003) is employed to estimate the WPF using all singular values (SVs) of matrix **Q**. This technique is particularly useful for inverting non-square or singular matrices, which do not have a standard inverse. To study the effect of the number of sensors on the estimation of the TBL WPF, the mean absolute error (MAE) of the estimated WPF in the low-wavenumber domain is calculated for different number of sensors with respect to the corresponding domain of the reference input TBL model simulated using the Goody and Mellen Models. The following formula is used to compute the MAE of the estimated WPF in the low-wavenumber domain

$$\mathrm{MAE} = \frac{1}{N_{k_{LW}}} \sum_{l=1}^{N_{k_{LW}}} |10\mathbf{log}_{10}\phi^{\mathrm{e}}_{pp}(k_{x,l}, k_{y,l}, \omega) - 10\mathbf{log}_{10}\phi^{\mathrm{r}}_{pp}(k_{x,l}, k_{y,l}, \omega)|, \tag{21}$$

where $N_{k_{LW}}$ correspond to the total number of grid points in the low-wavenumber domain. $\phi^{\mathrm{e}}_{pp}(k_{x,i}, k_{y,j}, \omega)$ and $\phi^{\mathrm{r}}_{pp}(k_{x,i}, k_{y,j}, \omega)$ are the estimated and reference CSD of the WPF, respectively. It should be noted that unlike the acoustic-based approach, where the co-array factor and sensor locations were crucial for estimating WPF in the low-wavenumber domain (Abtahi et al., 2024), our investigation (results are not shown here) showed that in the vibration-based approach the estimation of WPF in the low-wavenumber domain is almost independent from the sensor positions and co-array factor.

Fig. 6 depicts the MAE of the estimated WPF in the low-wavenumber domain as a function of the number of sensors at some selected frequencies. For the results in Fig. 6, the WPF is evaluated by applying the Moore–Penrose pseudo-inverse method to obtain the inverse of the matrix **Q** in Eq. (12) using all SVs of matrix **Q**. In the case of a rectangular plate, two mode numbers are necessary in both the x-direction and the y-direction to label each vibration mode. Upon examining the mode numbers and referring to Fig. 6, it is found that for a given frequency of excitation, as the number of sensors approaches the sum of maximum mode number of the plate along x and y directions below the excitation frequency ($M_b + N_b$), a notable increase in the MAE is manifested. The vertical dashed lines show this sum for each frequency. This observation leads to the conclusion that to avoid a dramatic increase in MAE while using the Moore–Penrose pseudo-inverse with all singular values (SVs), the maximum number of sensors should be limited to the $M_b + N_b$ at the excitation frequency. However, the condition number for the matrix norm of **Q** in Eq. (12) is very large, classifying it as severely ill-conditioned (Hansen, 2007). This condition implies that even a small perturbation in the input data can lead to a significant impact on the solution, rendering the equation without a unique solution (Hansen, 2007). Therefore, as can be seen from Fig. 6, the MAE is still large even when the above threshold is considered. This suggests that an alternative approach must be explored to achieve a more accurate estimation of the WPF in the low-wavenumber domain.

3.1.2. Truncated generalized singular value decomposition method

To improve the accuracy of the WPF estimation in the low-wavenumber domain, numerical regularization methods have been used for computing stabilized solutions for discrete ill-posed problems. The goal of regularization theory is to provide appropriate side constraints with optimal weights so that the regularized solution is a suitable approximation of the unknown desired solution. These methods filter out contributions to the solution that correspond to small singular values, but there is no specific procedure that can solve every individual problem (Hansen, 2007).

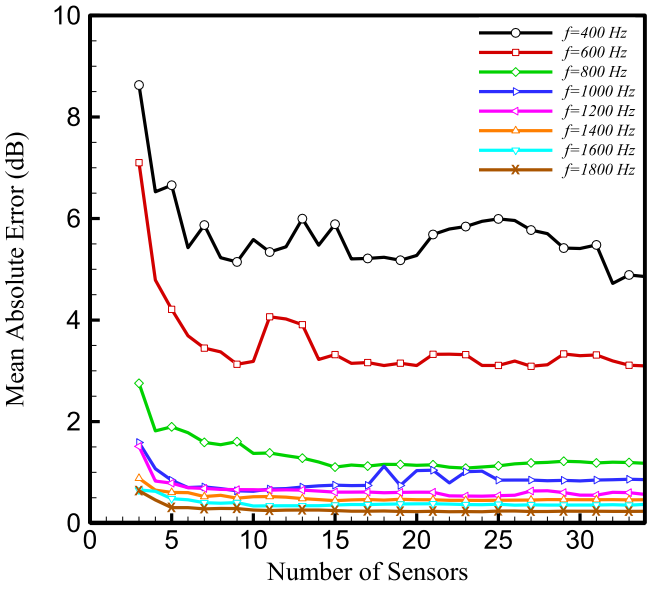

Fig. 7. MAE for estimated WPF in the low-wavenumber domain as a function of sensor number at some selected frequencies using the truncated generalized singular value decomposition method.

We used various regularization techniques described in Hansen (2007) to compute the WPF through Eq. (12). The truncated generalized singular value decomposition (TGSVD) method was found to be more effective in estimating the WPF in the low-wavenumber domain by minimizing the first derivative 2-norm of the solution (Hansen, 2007). The regularization parameter for truncating the generalized singular value problem is determined using the corner method, considering a minimum of 4 sensors for the array arrangement. This method employs an adaptive pruning algorithm to identify the corner of a discrete L-curve generated by the TGSVD method (Hansen et al., 2007). For the numerical applications presented herein, the Matlab package developed by Hansen (2007) for the analysis and solution of discrete ill-posed problems was utilized (see Abtahi et al. (2024)).

Similar to Fig. 6, Fig. 7 illustrates the MAE as a function of sensor numbers at selected frequencies using the TGSVD method. Based on the observations made earlier in Fig. 6 concerning the relationship between the mode numbers and the number of SVs used for the inversion of matrix **Q**, it is essential to restrict the number of SVs to the sum of maximum mode number of the plate along x and y directions below each frequency of excitation (M_b+N_b) when a higher number of SVs can be employed for WPF estimation. It is worth mentioning that for an array with N_s sensors, N_s^2 CSD can be computed. Thus, the number of SVs in matrix **Q** is equivalent to N_s^2. Using this observation, we set a preconditioning for determining the regularization parameter using the corner method: if the number of sensors in the array arrangement is lower than $M_b + N_b$ at the exciting frequency, all SVs are used for regularization parameter determination. However, if the number of sensors exceeds $M_b + N_b$, the regularization parameter is determined using the first $(M_b + N_b)^2$ SVs. The results depicted in Fig. 7 reveal that the utilization of the TGSVD method consistently yields lower MAE at each frequency when compared to Fig. 6, even for $N_s \leq (M_b + N_b)$. Additionally, this figure highlights that the calculated MAE is lower at higher frequencies compared to the corresponding MAE values at lower frequencies. This suggests that as we move further away from the coincidence frequency, the panel's vibration is dominated by the low-wavenumber components of the WPF, resulting in a more precise estimation of the WPF. Furthermore, for frequencies beyond 1000 Hz, the MAE remains below 1 dB when utilizing only 5 sensors, and increasing the number of sensors does not result in a substantial enhancement in the estimation of the low-wavenumber WPF. Consequently, in contrast to the acoustic-based approach (Abtahi et al., 2024), employing a relatively small number of sensors in the vibration-based method is sufficient for accurate estimation of the WPF in the low-wavenumber domain.

In what follows, we showcase the results of the WPF estimation in the low-wavenumber domain and the corresponding MAE calculations using the TGSVD method. The outlined procedure from the preceding subsections is applied at two selected frequencies: 1400 Hz (non-resonance frequency) and 1511 Hz (resonance frequency). We use a wavenumber resolution of $\delta k_x = \delta k_y = 5.6$ m^{-1} for the resonance frequency, and a resolution of 6.1 m^{-1} for non-resonant frequencies. Fig. 8(a), (b) illustrate the CSD of the TBL WPF generated using the Goody+Mellen model as the reference input at 1400 Hz and 1511 Hz, respectively. The targeted low-wavenumber domain is represented by a rectangular area in Fig. 8(a), (b).

Fig. 8(c)–(f) present the estimated WPF obtained by applying the TGSVD method to the CSM of acceleration data collected from an irregular arrangement of 10 sensors mounted on the TBL-excited panel at resonance and non-resonance frequencies. Fig. 8(c),(d) present a color map of the estimated WPF. Fig. 8(e),(f) provide cross-sectional views of both the reference and estimated WPF at $k_y = 0$, with two red-dashed lines indicating the boundaries of the low-wavenumber domain. Additionally, the calculated MAEs between the reference input WPF and estimated WPF in the low-wavenumber domain for $f = 1400$ Hz and $f = 1511$ Hz are 0.52 dB and 0.32 dB, respectively. The results depicted in Fig. 8(c)–(f) demonstrate that by following the procedure outlined in Section 2 and

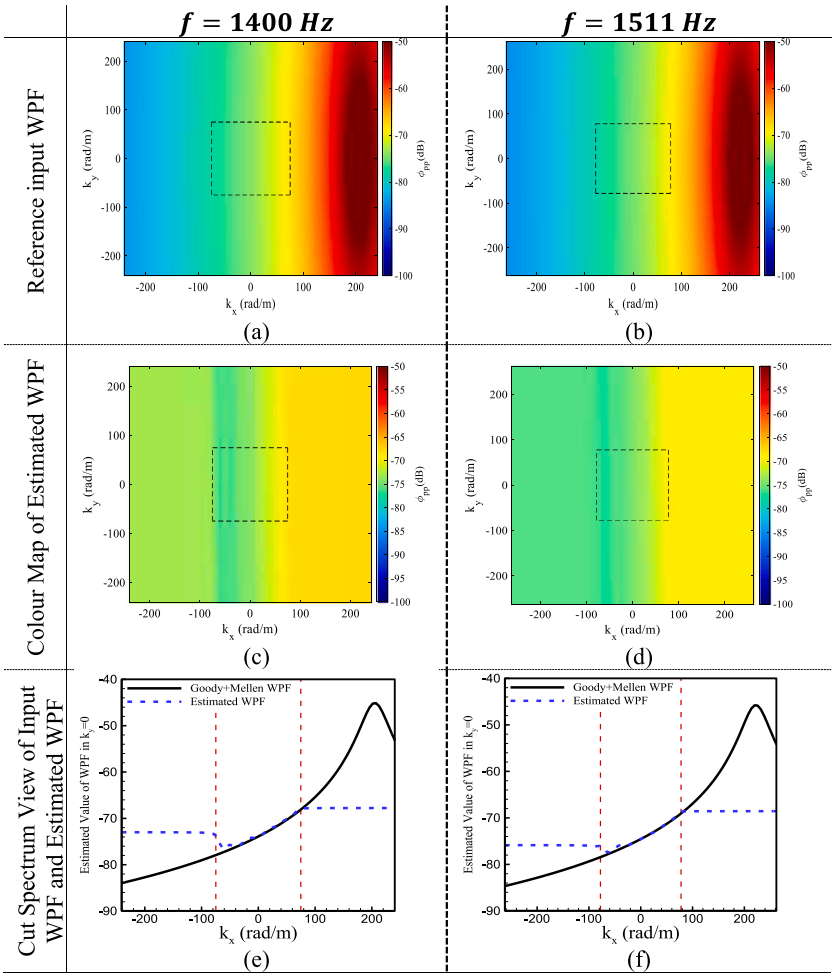

Fig. 8. Evaluation of the proposed method on the estimation of WPF in the low-wavenumber domain at 1400 Hz (left column) and 1511 Hz (right column) using a random array pattern with 10 sensors. Reference input CSDs of WPF for each frequency are shown in (a) and (b), and map view of the estimated WPF are presented in (c) and (d). 2D wavenumber-frequency spectra for $k_y = 0$ are plotted against longitudinal wavenumber in (e) and (f). MAEs calculated between the reference input CSD and estimated WPF in the low-wavenumber domain for f = 1400 Hz and f = 1511 Hz are 0.52 dB and 0.32 dB, respectively. (For interpretation of the references to color in this figure legend, the reader is referred to the web version of this article.)

utilizing an irregular array consisting of 10 sensors, it is possible to accurately estimate the WPF in the low-wavenumber domain, with an MAE below 1 dB. It can also be observed that when the excitation frequency is sufficiently distant from the coincidence frequency, the panel filters the convective region of the WPF. Hence, the panel vibration is mostly due to the low-wavenumber domain of the WPF. As a result, the proposed method could estimate the WPF within the low-wavenumber domain accurately, while the WPF outside of this domain cannot be effectively estimated.

3.1.3. Improving the accuracy of low-wavenumber WPF estimation at low frequencies

As shown in Fig. 7, the calculated MAE within the low-wavenumber domain of the WPF at lower frequencies (f = 400 Hz and f = 600 Hz) is higher compared to that at higher frequencies due to the proximity to the coincidence frequency. To enhance the accuracy of the estimated WPF within the low-wavenumber domain for these particular frequencies, we explored the impact of modifying the panel's dimensions, as illustrated in Fig. 9. This involves considering a scaling ratio (SR) for the panel, where the L_x and L_y dimensions of the panel were multiplied by the SR value, and the positions of the sensors were adjusted or scaled accordingly. All other parameters were kept constant during this investigation. It is important to note that this modification does not affect the flexural wavenumber of the panel (as per Eq. (20)), ensuring that the targeted low-wavenumber domain for estimation remains unchanged. As observed in Fig. 9, increasing the SR results in enhanced estimations of the WPF and a subsequent reduction in the MAE. To provide rationale for this observation, Fig. 10 illustrates the MAE against $\beta = \mathrm{SR}\sqrt{A}/\lambda_b$ across multiple low frequencies (close to the coincidence frequency). Here, A represents the surface area of the original plate ($L_x \times L_y$), and $\lambda_b = 2\pi/k_b$ denotes the flexural wavelength of the plate at the excitation frequency. This ratio signifies the number of wavelengths present in the plate

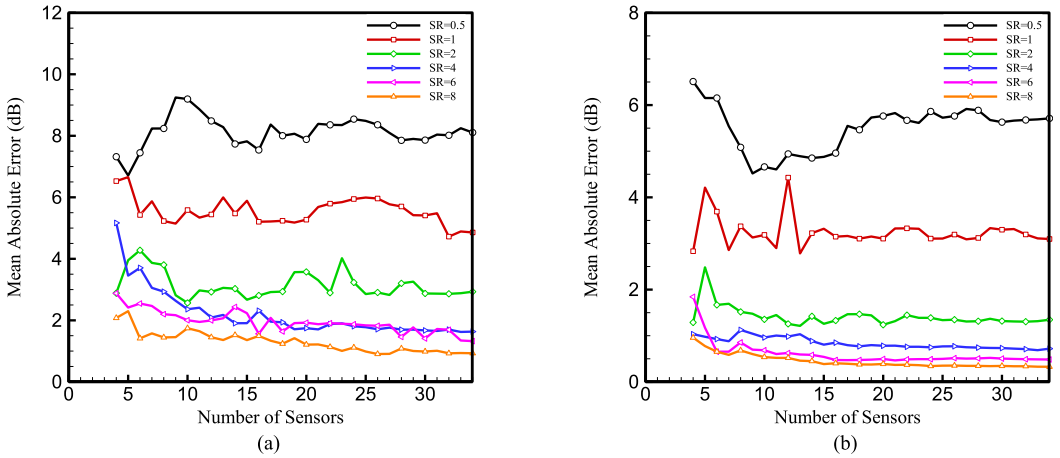

Fig. 9. Comparison of the MAE for the estimated WPF in the low-wavenumber domain at (a) 400 Hz and (b) 600 Hz as a function of number of sensors for different scaling ratio values.

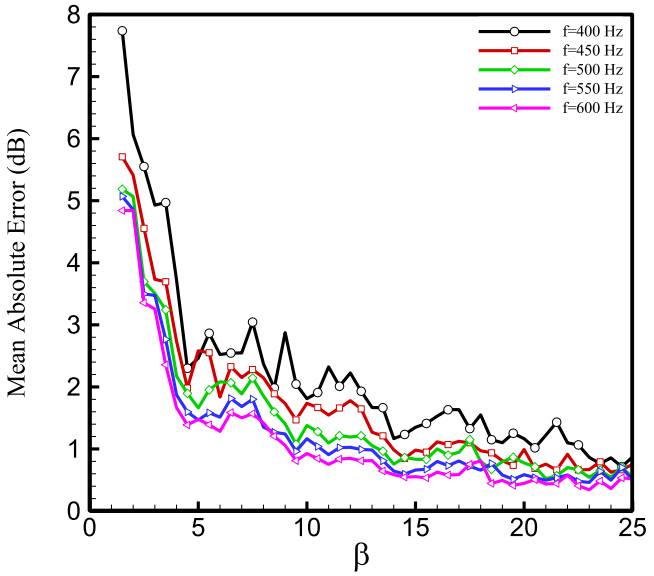

Fig. 10. Comparison of the MAE for the estimated WPF in the low-wavenumber domain at low frequencies as a function of $\beta = \mathrm{SR}\sqrt{A}/\lambda_b$.

at each frequency. As it can be seen from Fig. 10, with a low number of flexural wavelengths ($\beta \leq 5$), the magnitude of MAE is notable. However, with an increase in β, the MAE decreases across the selected frequencies. Particularly at high β values, the MAE converges to a level below 1 dB. This trend implies that employing larger panels with $\beta > 5$, which accommodate a greater number of flexural wavelengths of the plate, leads to improved WPF estimations at low-frequencies.

3.2. Virtual vibration experiments

In Section 3.1, we used a closed-form formula for the CSD function of the WPF and employed the vibration of a panel excited by the forcing function based on this WPF to estimate the input WPF through an inverse method. A parametric study was then carried out to better understand the effect of each system's parameter on the WPF estimation. However, in practice, such a closed-form WPF does not exist. Even when multiple records of the pressure fluctuations are obtained under the same experimental conditions, they would not be identical due to the random nature of excitation. Each outcome of an experiment involving random processes is known as a sample function, and the collective set of potential outcomes is referred to as the ensemble of the process. In order to have a more realistic assessment of the effectiveness of the proposed method for estimating the WPF, a virtual vibration experiment is conducted. This involves simulating the WPF using various deterministic realizations of TBL pressure fluctuations, and then estimating the CSM

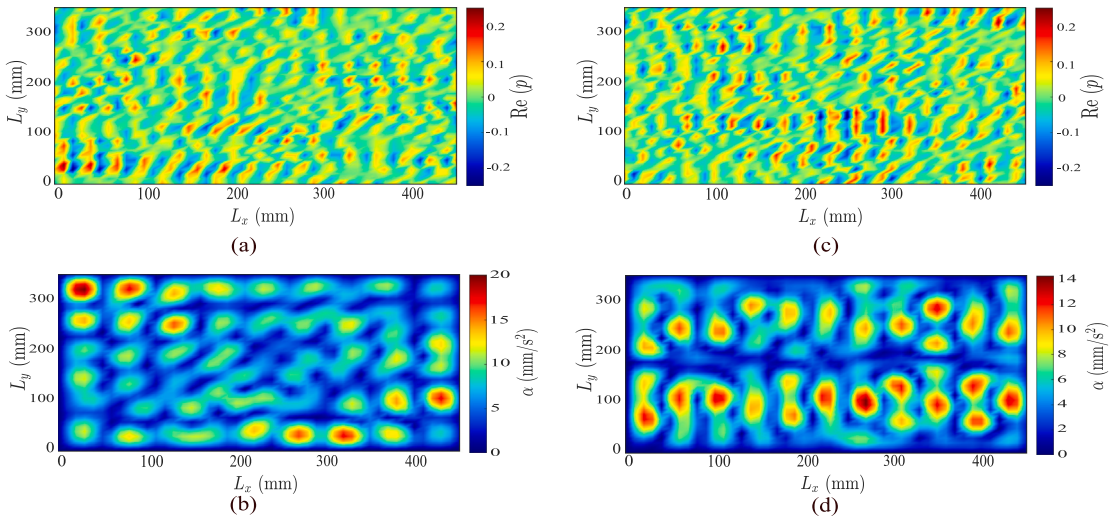

Fig. 11. Two realizations of the WPF at (a) 1400 Hz and (c) 1511 Hz using the truncated Mellen and Goody models for a flow speed of 50 m/s, accompanied by the corresponding panel displacement in (b) and (d).

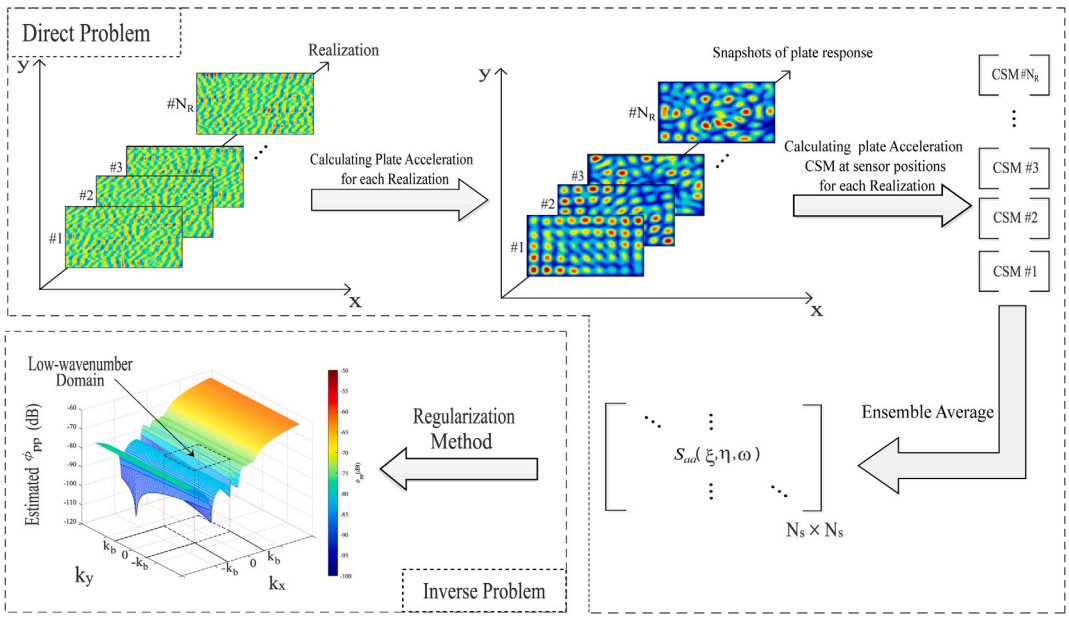

Fig. 12. Simulation process in the virtual vibration experiments using the UWPW technique.

through ensemble averaging of these realizations. To achieve this, the UWPW technique (Maxit, 2016) described in Section 2.3 is employed for simulating the WPF.

By employing multiple realizations, the acceleration response of the panel can be computed using Eq. (18) for each realization. As an illustration, Fig. 11 displays two realizations of the surface pressure field at frequencies of 1400 Hz and 1511 Hz, accompanied by their corresponding panel displacements. Different number of realizations is used in the ensemble averaging process to calculate the CSM of panel accelerations at the sensor positions. Subsequently, the CSM of the panel acceleration can be obtained by ensemble averaging of the calculated CSD of acceleration between different pairs of sensors across all realizations. Fig. 12 shows a flowchart describing the implementation of the UWPW technique in the virtual vibration experiment for estimation of the WPF in the low-wavenumber domain. This approach allows simulation and estimation of the WPF in a realistic manner.

In following subsection, we study the effect of the number of realizations as a function of the excitation frequency and number of sensors (Section 3.2.1) using the virtual vibration approach on the estimation of the WPF in the low-wavenumber domain.

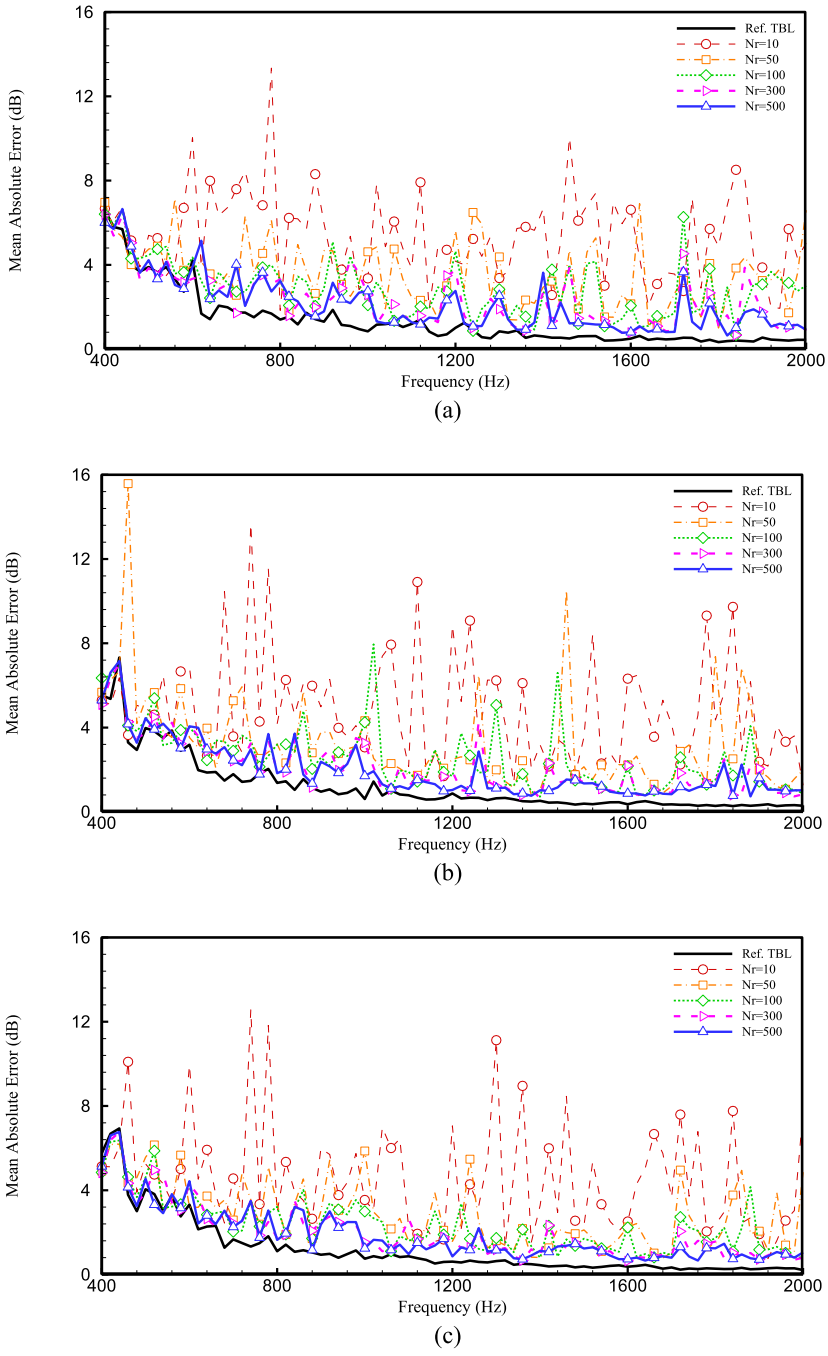

Fig. 13. Comparison of MAE for the estimated WPF in the low-wavenumber domain as a function of frequency. The results showcase the impact of the number realization on the accuracy of the estimated WPF for (a) $N_s = 5$, (b) $N_s = 10$, and (c) $N_s = 15$.

3.2.1. Effect of number of realizations

In this section, the impact of the number of realizations on the estimation of the WPF in the low-wavenumber domain is examined. Fig. 13 presents a comparison of the MAE values for the estimated WPF as a function of frequency using an irregular array pattern with numbers of sensors: $N_s = 5$, $N_s = 10$, and $N_s = 15$. In this figure, "Ref. TBL" represents the MAE computed using the closed-form formula. The MAE values are plotted for various numbers of realizations. The findings indicate that with an increase in the number of realizations, the MAE values converge towards the ideal case (Ref. TBL). Furthermore, the graph in Fig. 13 illustrates that MAE

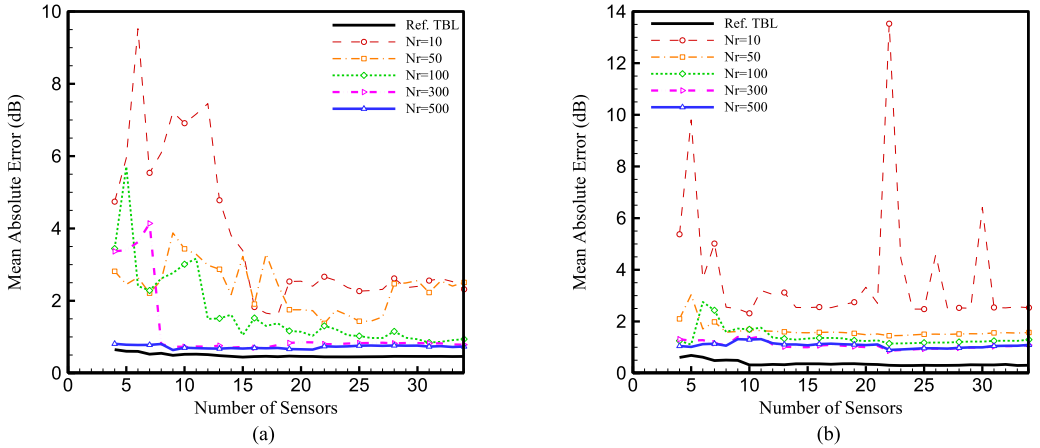

Fig. 14. Comparison of MAE for the estimated WPF in the low-wavenumber domain as a function of number of sensors. The results showcase the impact of the number realization on accuracy of the estimated WPF for (a) $f = 1400$ Hz and (b) $f = 1511$ Hz.

decreases at higher frequencies, indicating greater accuracy in estimating the WPF in the low-wavenumber domain. This observation underscores that the accuracy of the estimated WPF improves as the frequency of excitation deviates further from the coincidence frequency, whether it is at resonance or non-resonance frequencies.

In Fig. 14, the impact of the number of sensors on the estimation of the WPF in the low-wavenumber domain is examined at two frequencies: (1) the non-resonance frequency of $f = 1400$ Hz and (2) the resonance frequency of $f = 1511$ Hz. In this figure, the MAE is plotted as a function of the number of sensors for the selected frequencies for different number of realizations. These MAE values are compared with those obtained using the reference input TBL excitation (Ref. TBL). The results indicate that as the number of realizations increases, the MAE values approach the reference case. It is observed that to achieve an accurate estimation of the WPF at these two selected frequencies with MAE below 2 dB, more than 300 realizations are required. Furthermore, it is observed that when a high number of realizations is used, increasing the number of sensors does not result in a significant improvement in the estimated WPF.

The color-maps and cross-section views at $k_y = 0$ of the estimated WPF in the low-wavenumber domain at $f = 1400$ Hz and $f = 1511$ Hz using different number of realizations are demonstrated in Figs. 15 and 16, respectively. The MAE between input reference WPF (Fig. 8(a), (b)) and estimated WPF in the low-wavenumber domain is included for each case to assess the accuracy of the estimations.

Based on the results displayed in Figs. 15 and 16, it can be seen that with only ten realizations ($N_r = 10$), the MAE exceeds 5 dB at the non-resonance frequency, while at the resonance frequency, it is approximately 2 dB. However, as the number of realizations increases to $N_r = 100$, the estimated WPF improves at both frequencies, with the MAE dropping to 3 dB at the non-resonance frequency and 1.69 dB at the resonance frequency. Further increasing the number of realizations results in even more accurate estimations, bringing the estimated WPF closer to the reference WPF. Notably, for $N_r \geq 300$, the estimated WPF exhibits high accuracy, with an MAE of approximately 1 dB. When comparing Fig. 8(f) with Fig. 16(b), (d), and (f), slight discrepancies between the estimated WPF and the reference become apparent, especially in the lower end of the low-wavenumber domain. These differences could be attributed to the number of realizations used to estimate the CSM. They can be alleviated by increasing the number of realizations. Additionally, this observation corresponds with the findings presented in Fig. 13, indicating that regardless of whether the excitation is at resonance or non-resonance frequency, the accuracy of the estimated WPF at each number of realizations generally improves as the frequency of excitation deviates further from the coincidence frequency.

Furthermore, upon comparing the results obtained by Abtahi et al. (2024) with the above findings, it can be inferred that, unlike the acoustic-based approach where a substantial number of realizations is needed to accurately estimate the low-wavenumber levels in the TBL pressure field (due to contamination by the convective ridge), utilizing the vibration-based approach filters the convective region of the WPF, allowing for accurate estimation of the low-wavenumber WPF using a significantly smaller number of realizations.

3.2.2. Repeatability study of the virtual vibration experiment

The utilization of a random procedure in the UWPW technique to generate the phase in Eq. (19) introduces variability in the CSM of the acceleration data obtained for each realization of the panel. This variability has the potential to impact the MAE value of the estimated WPF in the low-wavenumber domain. To assess the influence of this factor on the WPF estimation, we considered four different numbers of realizations: $N_r = 50$, $N_r = 100$, $N_r = 200$, and $N_r = 300$. We calculated the vibration response of the panel at $f = 1400$ Hz and generated probability density function (PDF) graphs based on 100 data samples collected for three irregular arrays with $N_s = 5$, $N_s = 10$, and $N_s = 15$, as shown in Fig. 5. Fig. 17 displays the PDF graphs for these scenarios with mean value μ

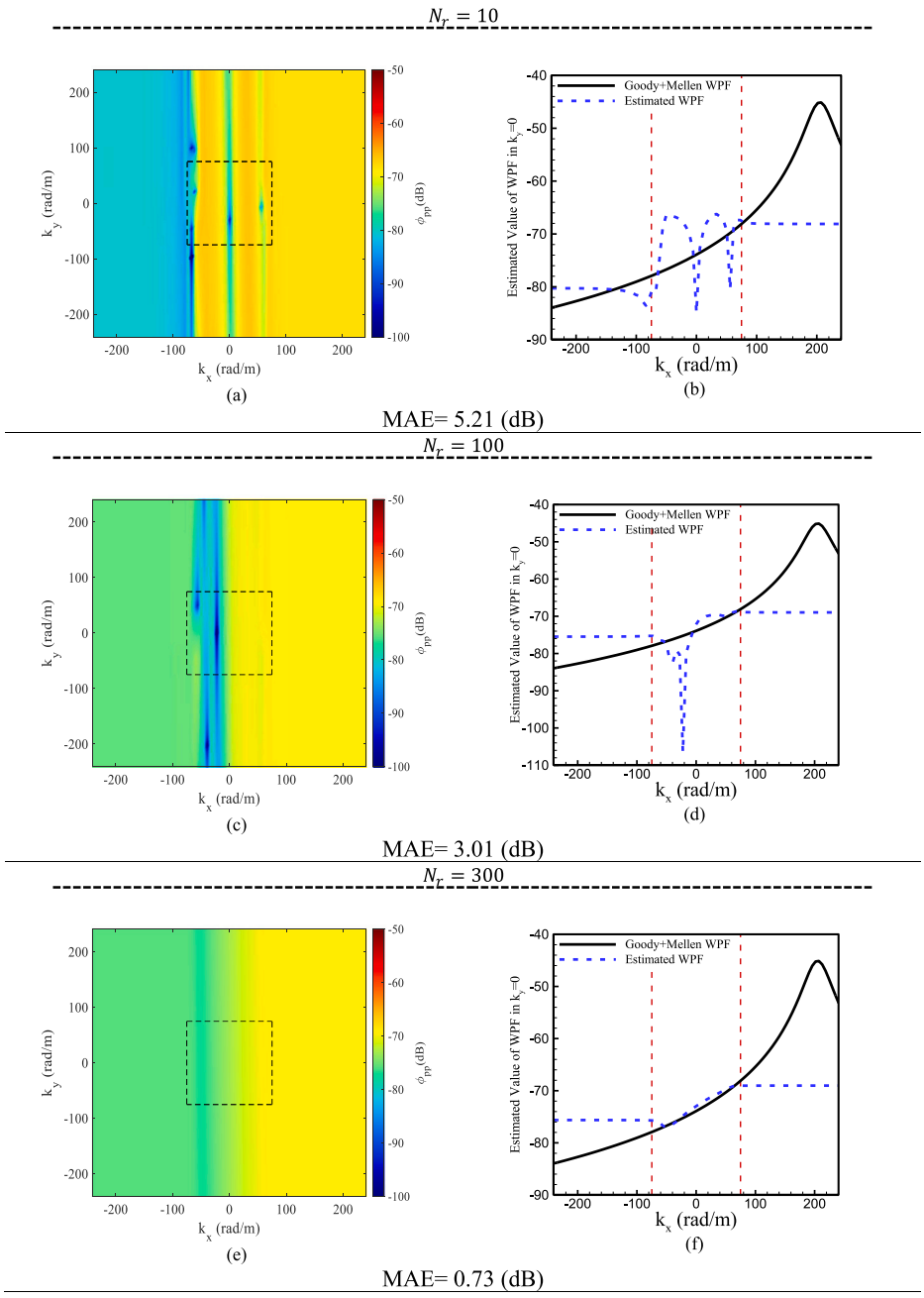

Fig. 15. The estimated WPF at f = 1400 Hz for an irregular array pattern with 10 sensors for different numbers of realizations. The left column shows the color maps of the estimated WPF, while the right column displays the 2D wavenumber-frequency spectra for $k_y = 0$. The MAE for each case is displayed in decibels (dB). (For interpretation of the references to color in this figure legend, the reader is referred to the web version of this article.)

of the collected samples. In the context of an experiment, this could be regarded as a repeatability study that measures the variation in the estimated output data under the same conditions.

This figure illustrates that the probability of encountering higher MAE values is significantly higher for the case with N_s = 5 and N_r = 50 compared to the other cases. However, as the number of sensors and realizations increase, the mean value μ of the samples decreases. This reduction indicates an improvement in the accuracy of the estimated WPF in the low-wavenumber domain. Additionally, the results presented in Fig. 17 underscore the robustness of employing the TGSVD method in the vibration-based

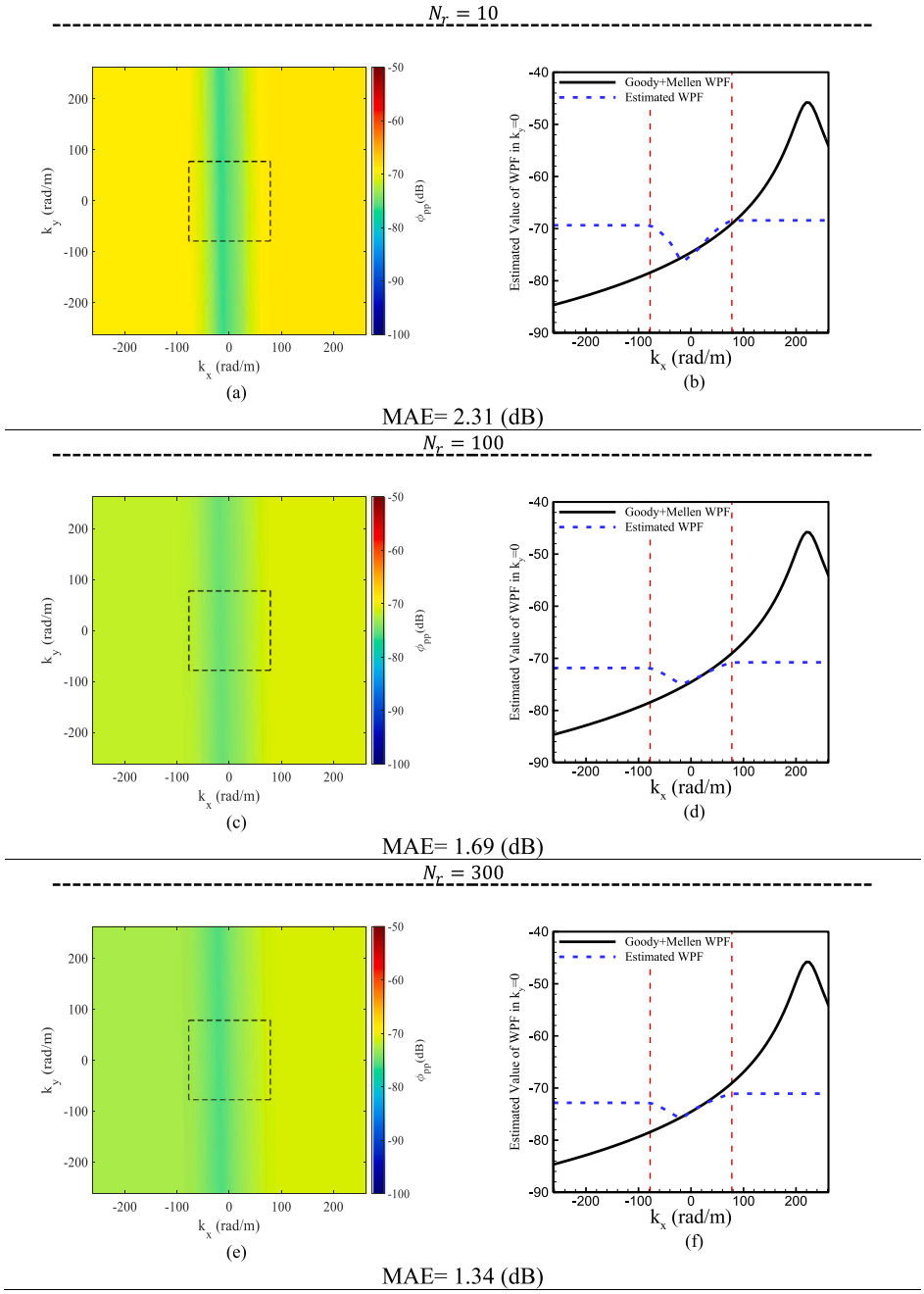

Fig. 16. The estimated WPF at $f = 1511$ Hz for an irregular array pattern with 10 sensors for different numbers of realizations. The left column shows the color maps of the estimated WPF, while the right column displays the 2D wavenumber-frequency spectra for $k_y = 0$. The MAE for each case is displayed in decibels (dB). (For interpretation of the references to color in this figure legend, the reader is referred to the web version of this article.)

approach, especially when a substantial number of realizations and a sufficiently high number of sensors are employed for the estimation of the WPF in the low-wavenumber domain. For instance, with $N_s = 15$ and $N_r = 300$, the majority of the calculated MAEs among 100 samples exhibit an accuracy below 1 dB, emphasizing the stability of the method.

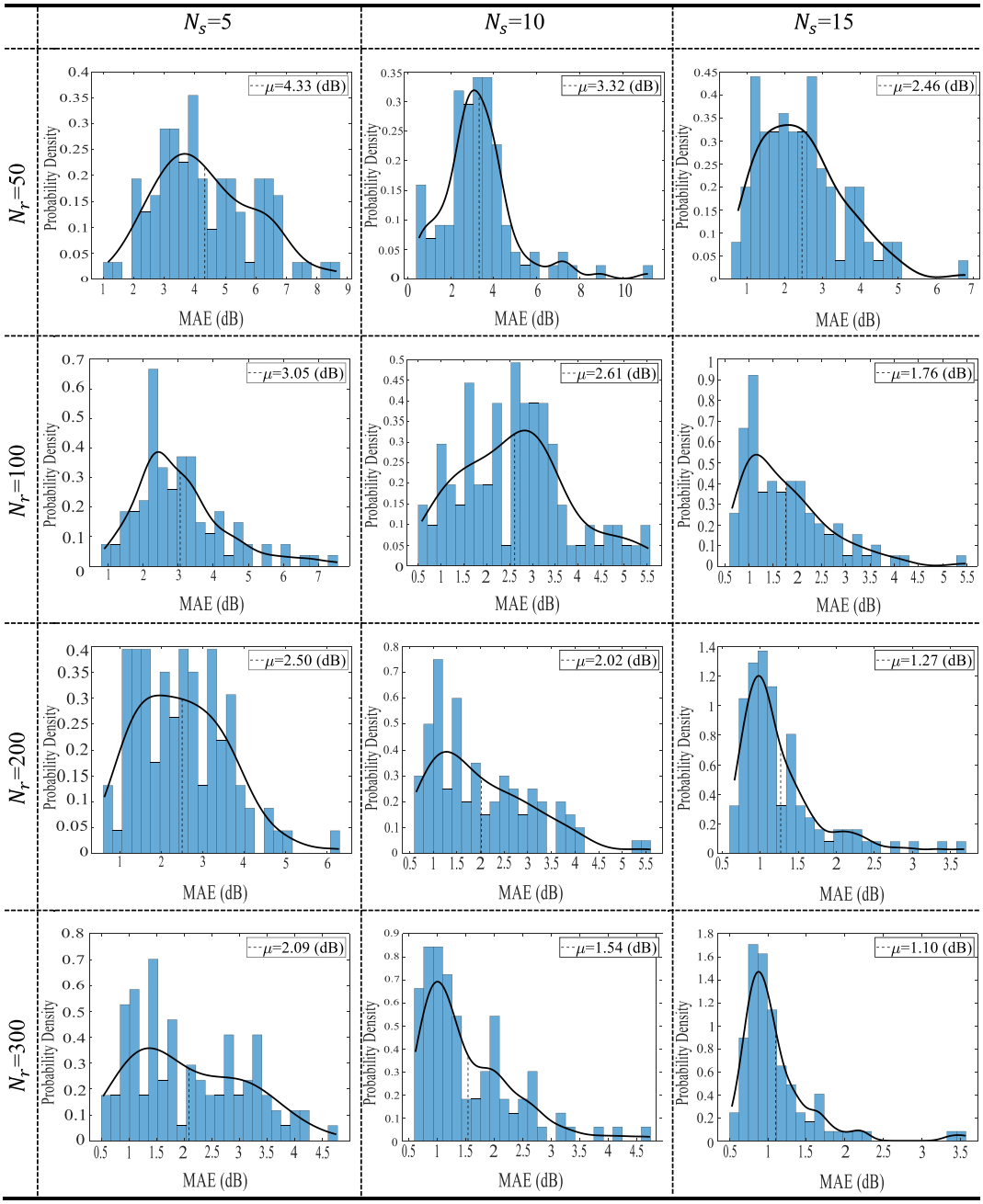

Fig. 17. The probability density function graphs showing the distribution of 100 samples obtained for different numbers of realizations at three irregular numbers of sensors.

4. Conclusions

In this study, an inverse vibration method for the estimation of the TBL WPF in the low-wavenumber domain was proposed. To demonstrate the efficacy of the method, an analytical model of an elastic simply-supported panel subjected to a TBL excitation was considered. Acceleration data acquired from the panel was then employed to estimate the WPF in the low-wavenumber domain. A parametric study was initially carried out using a closed-form TBL forcing function to show the effects of number of vibration sensors and size of the panel on the accuracy of the WPF estimation in the low-wavenumber domain. It was found that, unlike the acoustic-based methods, where a relatively high number of sensors is required to respect the Nyquist criterion, a few sensors are sufficient to estimate the WPF in the low-wavenumber using the proposed vibration-based method. Moreover, the error of the WPF

estimation in the low-wavenumber domain at low frequencies (close to the coincidence frequency) can be substantially reduced by increasing only the size of the panel without changing other parameters. This allows accurate estimation of the WPF over a wider frequency range.

Moreover, to quantify the potential effectiveness of the proposed method in practice, virtual experiments were conducted using the UWPW technique, where the CSM was approximated through an ensemble average of various realizations of the panel's acceleration induced by the WPF. This simulated a practical scenario where limited samples are available and can be collected from vibration measurements of the panel. It was realized that a few hundred snapshots were required for accurately estimating the WPF in the low-wavenumber domain. Additionally, to evaluate the repeatability of the proposed procedure in real experiments for estimating the WPF in the low-wavenumber domain, we considered different sets of realizations using the UWPW technique across various numbers of sensors. The obtained results demonstrated the effective and accurate performance of the proposed regularization method when a substantial number of realizations and an ample number of sensors were employed for estimating WPF in the low-wavenumber domain.

Nevertheless, it is important to note that this investigation was under the assumptions of having a homogeneous, stationary, and fully developed TBL with zero pressure gradient across the plate. Additionally, it was assumed that panel vibrations do not affect the WPF and that the random TBL force is ergodic. These simplifications underscore the difficulties in estimating this region in experiments, where not only homogeneity in the TBL and ergodic randomness may not hold true, but also various sources of error and uncertainties, including background noise, instrumental and human errors, exist.

CRediT authorship contribution statement

Hesam Abtahi: Writing – original draft, Validation, Software, Methodology, Investigation, Formal analysis, Data curation, Conceptualization. **Mahmoud Karimi:** Writing – review & editing, Supervision, Resources, Project administration, Methodology, Investigation, Conceptualization. **Laurent Maxit:** Writing – review & editing, Supervision, Methodology, Investigation, Conceptualization.

Declaration of competing interest

The authors declare that they have no known competing financial interests or personal relationships that could have appeared to influence the work reported in this paper.

Data availability

Data will be made available on request.

Acknowledgments

The first author acknowledges that this research is supported by the UTS President's Scholarship, Australia.

Appendix. Sensitivity function of a simply-supported panel

The sensitivity function $H_\gamma(\mathbf{x},\mathbf{k},\omega)$ for a simply-supported rectangular panel corresponding to the velocity at point $\mathbf{x}$ when the panel is excited by a unit wall plane wave is given by

$$H_\gamma(\mathbf{x},\mathbf{k},\omega) = -\omega^2 \sum_{m=1}^{M}\sum_{n=1}^{N} \frac{\psi_{mn}(\mathbf{k})\varphi_{mn}(\mathbf{x})}{\Omega(\omega_{mn}^2 - \omega^2 + \mathrm{j}\eta\omega\omega_{mn})}, \tag{A.1}$$

where $\Omega = \rho_s h L_x L_y/4$ is the modal mass, η is the structural loss factor, and M, N are the cut-off modal orders in the x and y directions, respectively. For a flat rectangular panel with simply-supported boundary conditions, ω_{mn} and $\varphi_{mn}(\mathbf{x})$ are respectively the modal frequency and mode shapes of the panel given by Rao (2019) and Karimi et al. (2020b)

$$\omega_{mn} = \sqrt{\frac{D}{\rho_s h}}\left(\left(\frac{m\pi}{L_x}\right)^2 + \left(\frac{n\pi}{L_y}\right)^2\right), \tag{A.2}$$

$$\varphi_{mn}(\mathbf{x}) = \sin\left(\frac{m\pi x}{L_x}\right)\sin\left(\frac{n\pi y}{L_y}\right), \tag{A.3}$$

where $D = Eh^3/(12(1-\nu^2))$ is the flexural rigidity, E is Young's modulus, and ν is Poisson's ratio. The modal forces ψ_{mn} are calculated by integration over the panel surface A as follows

$$\psi_{mn}(k_x,k_y) = \int_A \varphi_{mn}(x,y)e^{\mathrm{j}(k_x x + k_y y)}\,\mathrm{d}A = I_m^x(k_x)I_n^y(k_y), \tag{A.4}$$

and

$$I_s^r|(r,s) = (x,m)\vee(y,n) = \begin{Bmatrix} \left(\frac{s\pi}{L_r}\right)\frac{(-1)^s e^{\mathrm{j}(k_r L_r)}-1}{k_r^2 - \left(\frac{s\pi}{L_r}\right)^2} & k_r \neq \frac{s\pi}{L_r} \\ \frac{1}{2}\mathrm{j}L_r & \text{otherwise} \end{Bmatrix}. \tag{A.5}$$

References

Abtahi, H., Karimi, M., Maxit, L., 2024. On the challenges of estimating the low-wavenumber wall pressure field beneath a turbulent boundary layer using a microphone array. J. Sound Vib. 574, 118230. http://dx.doi.org/10.1016/j.jsv.2023.118230.

Arguillat, B., Ricot, D., Bailly, C., Robert, G., 2010. Measured wavenumber: Frequency spectrum associated with acoustic and aerodynamic wall pressure fluctuations. J. Acoust. Soc. Am. 128 (4), 1647–1655. http://dx.doi.org/10.1121/1.3478780.

Ben-Israel, A., Greville, T.N., 2003. Generalized Inverses: Theory and Applications, vol. 15, Springer Science & Business Media.

Blake, W.K., Chase, D.M., 1971. Wavenumber-frequency spectra of turbulent-boundary-layer pressure measured by microphone arrays. J. Acoust. Soc. Am. 49 (3B), 862–877. http://dx.doi.org/10.1121/1.1912427.

Bonness, W.K., Capone, D.E., Hambric, S.A., 2010. Low-wavenumber turbulent boundary layer wall-pressure measurements from vibration data on a cylinder in pipe flow. J. Sound Vib. 329 (20), 4166–4180. http://dx.doi.org/10.1016/j.jsv.2010.04.010.

Chase, D.M., 1980. Modeling the wavevector-frequency spectrum of turbulent boundary layer wall pressure. J. Sound Vib. 70 (1), 29–67. http://dx.doi.org/10.1016/0022-460X(80)90553-2.

Chase, D., 1992. Fluctuating wall-shear stress and pressure at low streamwise wavenumbers in turbulent boundary-layer flow at low Mach numbers. J. Fluids Struct. 6 (4), 395–413. http://dx.doi.org/10.1016/0889-9746(92)90023-V.

Ciappi, E., De Rosa, S., Franco, F., Hambric, S.A., Leung, R.C., Clair, V., Maxit, L., Totaro, N., 2021. Flinovia–Flow Induced Noise and Vibration Issues and Aspects-III. Springer.

Ciappi, E., Magionesi, F., De Rosa, S., Franco, F., 2009. Hydrodynamic and hydroelastic analyses of a plate excited by the turbulent boundary layer. J. Fluids Struct. 25 (2), 321–342. http://dx.doi.org/10.1016/j.jfluidstructs.2008.04.006.

Corcos, G., 1964. The structure of the turbulent pressure field in boundary-layer flows. J. Fluid Mech. 18 (3), 353–378. http://dx.doi.org/10.1017/S002211206400026X.

Damani, S., Braaten, E., Szoke, M., Alexander, W.N., Devenport, W.J., Balantrapu, N.A., Pearce, B.P., Starkey, T.A., Hibbins, A.P., Sambles, J.R., 2022. Resonator-based pressure sensor for wall pressure. In: 28th AIAA/CEAS Aeroacoustics 2022 Conference. p. 2956. http://dx.doi.org/10.2514/6.2022-2956.

Damani, S., Butt, H., Totten, E., Chaware, S., Sharma, B., Devenport, W.J., Lowe, T., 2024. The characteristics of sub-convective wall pressure fluctuations in a turbulent boundary layer. In: AIAA SCITECH 2024 Forum. p. 1904. http://dx.doi.org/10.2514/6.2024-1904.

Evans, N.D., Capone, D.E., Bonness, W.K., 2013. Low-wavenumber turbulent boundary layer wall-pressure measurements from vibration data over smooth and rough surfaces in pipe flow. J. Sound Vib. 332 (14), 3463–3473. http://dx.doi.org/10.1016/j.jsv.2013.01.028.

Farabee, T.M., Geib, F.E., 1975. Measurement of boundary layer pressure fields with an array of pressure transducers in a subsonic flow. In: ICIASF'75. pp. 311–319.

Geib, F., Farabee, T., 1976. Measurement of boundary layer pressure fluctuations at low wavenumber on smooth wall. J. Acoust. Soc. Am. 59 (S1), http://dx.doi.org/10.1121/1.2002710, S45–S45.

Goody, M., 2004. Empirical spectral model of surface pressure fluctuations. AIAA J. 42 (9), 1788–1794. http://dx.doi.org/10.2514/1.9433.

Graham, W., 1996. Boundary layer induced noise in aircraft, Part I: The flat plate model. J. Sound Vib. 192 (1), 101–120. http://dx.doi.org/10.1006/jsvi.1996.0178.

Graham, W., 1997. A comparison of models for the wavenumber–frequency spectrum of turbulent boundary layer pressures. J. Sound Vib. 206 (4), 541–565. http://dx.doi.org/10.1006/jsvi.1997.1114.

Guyader, J.-L., 2013. Vibration in Continuous Media. John Wiley & Sons.

Hambric, S.A., Hwang, Y.F., Bonness, W.K., 2004. Vibrations of plates with clamped and free edges excited by low-speed turbulent boundary layer flow. J. Fluids Struct. 19 (1), 93–110. http://dx.doi.org/10.1016/j.jfluidstructs.2003.09.002.

Hansen, P.C., 2007. Regularization tools version 4.0 for Matlab 7.3. Numer. Algorithms 46 (2), 189–194. http://dx.doi.org/10.1007/s11075-007-9136-9.

Hansen, P.C., Jensen, T.K., Rodriguez, G., 2007. An adaptive pruning algorithm for the discrete L-curve criterion. J. Comput. Appl. Math. 198 (2), 483–492. http://dx.doi.org/10.1016/j.cam.2005.09.026.

Hwang, Y., Bonness, W., Hambric, S., 2003. On Modeling Structural Excitations by Low Speed Turbulent Boundary Layer Flows. Technical Report, Pennsylvania State Univ State College Applied Research Lab.

Hwang, Y., Bonness, W.K., Hambric, S.A., 2009. Comparison of semi-empirical models for turbulent boundary layer wall pressure spectra. J. Sound Vib. 319 (1–2), 199–217. http://dx.doi.org/10.1016/j.jsv.2008.06.002.

Hwang, Y., Maidanik, G., 1990. A wavenumber analysis of the coupling of a structural mode and flow turbulence. J. Sound Vib. 142 (1), 135–152. http://dx.doi.org/10.1016/0022-460X(90)90587-P.

Jameson, P., 1970. Measurement of low wavenumber component of turbulent boundary layer wall pressure spectrum. Rap. tech. BBN Rep (1937).

Jameson, P., 1975. Measurement of the low-wavenumber component of turbulent boundary layer pressure spectral density. https://scholarsmine.mst.edu/sotil/22/.

Juvé, D., Prigent, S.L., Salze, E., Souchotte, P., Bailly, C., 2019. Opening lectures—Wall-pressure wavenumber-frequency spectra: Experimental challenges and recent advances. In: International Conference on Flow Induced Noise and Vibration Issues and Aspects. Springer, pp. 1–23. http://dx.doi.org/10.1007/978-3-030-64807-7_1.

Karimi, M., Croaker, P., Maxit, L., Robin, O., Skvortsov, A., Marburg, S., Kessissoglou, N., 2020a. A hybrid numerical approach to predict the vibrational responses of panels excited by a turbulent boundary layer. J. Fluids Struct. 92, 102814. http://dx.doi.org/10.1016/j.jfluidstructs.2019.102814.

Karimi, M., Croaker, P., Skvortsov, A., Moreau, D., Kessissoglou, N., 2019. Numerical prediction of turbulent boundary layer noise from a sharp-edged flat plate. Int. J. Numer. Methods Fluids 90 (10), 522–543. http://dx.doi.org/10.1002/fld.4733.

Karimi, M., Maxit, L., Croaker, P., Robin, O., Skvortsov, A., Marburg, S., Atalla, N., Kessissoglou, N., 2020b. Analytical and numerical prediction of acoustic radiation from a panel under turbulent boundary layer excitation. J. Sound Vib. 479, 115372. http://dx.doi.org/10.1016/j.jsv.2020.115372.

Keith, W.L., Hurdis, D., Abraham, B., 1992. A comparison of turbulent boundary layer wall-pressure spectra. J. Fluids Eng. 114, 338–347. http://dx.doi.org/10.1115/1.2910035.

Lecoq, D., Pezerat, C., Thomas, J.-H., Bi, W., 2014. Extraction of the acoustic component of a turbulent flow exciting a plate by inverting the vibration problem. J. Sound Vib. 333 (12), 2505–2519. http://dx.doi.org/10.1016/j.jsv.2014.02.003.

Maidanik, G., 1967. Flush-mounted pressure transducer systems as spatial and spectral filters. J. Acoust. Soc. Am. 42 (5), 1017–1024. http://dx.doi.org/10.1121/1.1910683.

Martin, N., Leehey, P., 1977. Low wavenumber wall pressure measurements using a rectangular membrane as a spatial filter. J. Sound Vib. 52 (1), 95–120. http://dx.doi.org/10.1016/0022-460X(77)90391-1.

Maury, C., Gardonio, P., Elliott, S., 2002. A wavenumber approach to modelling the response of a randomly excited panel, part I: general theory. J. Sound Vib. 252 (1), 83–113. http://dx.doi.org/10.1006/jsvi.2001.4028.

Maxit, L., 2016. Simulation of the pressure field beneath a turbulent boundary layer using realizations of uncorrelated wall plane waves. J. Acoust. Soc. Am. 140 (2), 1268–1285. http://dx.doi.org/10.1121/1.4960516.

Mellen, R.H., 1990. On modeling convective turbulence. J. Acoust. Soc. Am. 88 (6), 2891–2893. http://dx.doi.org/10.1121/1.399695.

Miller, T.S., Gallman, J.M., Moeller, M.J., 2012. Review of turbulent boundary layer models for acoustic analysis. J. Aircr. 49 (6), 1739–1754. http://dx.doi.org/10.2514/1.C031405.

Rao, S.S., 2019. Vibration of Continuous Systems. John Wiley & Sons.
Smol'yakov, A., 2000. Calculation of the spectra of pseudosound wall-pressure fluctuations in turbulent boundary layers. Acoust. Phys. 46 (3), 342–347. http://dx.doi.org/10.1134/1.29890.
Smol'Yakov, A., 2006. A new model for the cross spectrum and wavenumber-frequency spectrum of turbulent pressure fluctuations in a boundary layer. Acoust. Phys. 52, 331–337. http://dx.doi.org/10.1134/S1063771006030146.